

Construction of First Principle Based Adiabatic and Diabatic Hamiltonian for TiO_6^{8-} unit of BaTiO_3 Crystal: Photoemission Spectra and Ferroelectricity

Mantu Kumar Sah^a, Soumya Mukherjee^{a,b}, Satyam Ravi^c and Satrajit Adhikari^{a,*}

^aSchool of Chemical Sciences,

Indian Association for the Cultivation of Science, Jadavpur, Kolkata - 700032, India

^bDepartment of Chemistry, MANIT, Bhopal, India

^cSchool of Advanced Sciences, VIT Bhopal University, Bhopal, India

May 6, 2025

Abstract

The ferroelectric property of BaTiO_3 crystal arises from the strong Pseudo Jahn-Teller (PJT) interactions between the non-degenerate ground electronic state, $^1A_{1g}$ and the degenerate $^1T_{1u}$ symmetry states through the nuclear distortions of t_{1u} modes in TiO_6^{8-} unit. In a d^0 electronic configuration of Ti^{4+} ion, the PJT interaction leads to a stabilization effect, which has been explored using Beyond Born-Oppenheimer (BBO) theory. The $^1T_{1u}$ excited states form a three-state degeneracy, exhibiting feeble Jahn-Teller (JT) distortions over the t_{2g} planes. For the first time, we compute *ab initio* adiabatic potential energy surfaces (PESs) and non-adiabatic coupling terms (NACTs), and thereafter, diabatic PESs and couplings for the perovskite unit, TiO_6^{8-} . Using a Time-Dependent Discrete Variable Representation (TDDVR) approach, the theoretical photoemission spectra exhibit good agreement with the experimental ones. Moreover, the experimental observation on order parameter associated with ferroelectric properties of BaTiO_3 crystal show close resemblance with present and other theoretical predictions.

*Author to whom correspondence should be addressed: e-mail: pcsa@iacs.res.in

1 Introduction

Over the last few decades, the electronic structure and various spectral properties of TiO_6^{8-} unit of BaTiO_3 crystal raised immense interest to the allied scientific community due to its prominent ferroelectric properties originated from strong Pseudo Jahn-Teller (PJT) interactions between the ground electronic state ($^1A_{1g}$) and the excited ones ($^1T_{1u}$). In other words, the profound non-adiabatic couplings among the electronic states ($^1A_{1g}$ and $^1T_{1u}$) play an important role for depicting the ferroelectric properties and complex spectral features. In the late sixties, I. B. Bersuker¹ first depicted that the adiabatic potential energy surfaces (PESs) of TiO_6^{8-} unit contains eight (8) minima over the planes constituted with t_{1u} symmetric normal modes corresponding to eight distorted nuclear configurations. At $T = 0\text{ K}$, the TiO_6^{8-} unit gets trapped in any one of those minima, whereas at higher temperature, that moiety gains sufficient energy to overcome the energy barrier between two minima and therefore, the averaging of all the eight structures associated with those minima leads to an undistorted octahedral nuclear configuration. Such nuclear displacements destroy the inversion symmetry of the octahedral unit leading to temperature dependent phases and spontaneous crystal polarisation, namely, ferroelectricity.

The TiO_6^{8-} unit of BaTiO_3 crystal remains a long standing interest for theoreticians as well as experimentalist due to its PJT active $^1A_{1g}$ symmetric ground state (originated from d^0 electronic configuration) interacting with triply degenerate excited one, $^1T_{1u}$. Koleżyński and co-worker² calculated the band structure of BaTiO_3 crystal using FP LAPW approach as implemented in WIEN2k program, which depicts broad dispersion of the valence band (about 5 eV) and a narrow forbidden energy gap (about 2 eV). Such calculations were carried out for cubic and tetragonal structures of the crystal so that the changes in the electronic structure due to the ferroelectric phase transition could be investigated. Moreover, their work explored the role of π bonds of oxygen atoms in the ferroelectric behaviour of the material. On the other hand, Qi-Jun Liu and co-workers³ performed density functional theory (DFT) calculations to determine the structural, electronic and optical properties of various phases as well as molecular-orbital bonding of the titled system, where the calculated ground state energies, relative stability and structural parameters show good agreement with the experimental results. Later on, Polinger *et al.*⁴ studied the origin of dipolar distortion of the titled system using Green's function method augmented by DFT based computations, where

it was depicted that those ferroelectric distortions are mainly originated from PJT effects between ground and excited electronic states of opposite parity. In addition, their work unveiled that multi-center long-range dipole-dipole interactions and their magnitudes are governed by the PJT effects. In the subsequent works, I. B. Bersuker predicted⁵ that the local distortions due to PJT interactions are dynamic in nature, but there would be a static dipole moment resulting into polarization and enhanced flexoelectricity. All the theoretical investigations considering several properties of PJT active perovskite systems, namely, ferroelectricity, multiferroicity, permittivity and flexoelectricity are summarized in the recently published review articles⁶. On the other hand, to understand the origin of ferroelectric instability in perovskite materials, Cohen *et al.*^{7,8} performed comprehensive self-consistent total energy calculations using the linearized augmented plane wave (LAPW) method within the local density approximation (LDA). Their findings on BaTiO₃ revealed that the hybridization of Ti 3d and O 2p states is crucial for the $Ti-O$ interaction, which drives ferroelectric instability. Furthermore, Junquera and Ghosez⁹ showed that ferroelectric instability of thin films of BaTiO₃ requires a minimum thickness of about 6 unit cells (about 24 Å), below which off-centre instability does not occur. Later on, García-Lastra *et al.*¹⁰ investigated both local and cooperative effects on ferroelectricity in BaTiO₃ using DFT-based LDA calculations. Such an investigation explored the external condition (like pressure) for the movement of single Ti^{4+} ion from the centre depicting the cooperative effects on the modulation of ferroelectricity.

In the last two decades, few theoretical investigations were carried out on the effects of spin-orbit (SO) coupling in metal and metal oxide doped BaTiO₃ crystals. Mirhosseini *et. al*¹¹ attempted to explore the presence of Rashba spin-orbit coupling in the 6p states of a Bi adlayer on BaTiO₃ (001), where electric polarization originated from the ferroelectricity of BaTiO₃ is mainly responsible for such SO couplings. Later on, Zhong and coworkers¹² extended such approach for Ba(Os,Ir,Ru)O₃ doped BaTiO₃ crystals, where giant Rashba SO splittings were unveiled and even monitored by an external electric field. Moreover, structural, electronic, magnetic and mechanical properties of the mixed perovskites (BiFeO₃ and BaTiO₃) were investigated using DFT based approaches, which depict strong SO effects in BiFeO₃ due to BaTiO₃ crystal.¹³ On the other hand, theoretical study of SO coupling in pure BaTiO₃ crystal is yet an unexplored area.

Several experimental groups^{14–19} were also involved to reveal the unique properties of perovskite

systems like TiO_6^{8-} with d^0 electronic configuration. In the late sixties, Pinczuk *et al.*¹⁴ determined the symmetries and frequencies of various Raman active vibrational modes of BaTiO_3 crystal using various scattering geometries. Turik and Shevchenko¹⁵ measured its dielectric spectra over a wide range of frequencies (10^3 to 10^{10} Hz), where the dielectric permittivity (ϵ_{33}) of the single-domain crystal undergoes a sharp jump around 10^7 Hz indicating the phase transition of BaTiO_3 crystal. The ultraviolet photoemission spectroscopy (UPS) of the valence electronic level, with a photon energy ($h\nu$) of 105 eV, was conducted on sputtered and annealed single crystal of BaTiO_3 by B. Cord and R. Courths.¹⁶ Other groups^{17,18} have performed X-ray diffraction studies as well as recorded X-ray photoelectron spectra of the BaTiO_3 thin films, which contain ions of various oxidation states of titanium atoms, namely, Ti^{2+} , Ti^{3+} and Ti^{4+} . In a recent work, Wan *et al.*¹⁹ investigated the low frequency dielectric and optical properties of powdered BaTiO_3 using terahertz time-domain spectroscopy (THz-TDS), which clearly indicates that the dielectric constant of BaTiO_3 has a strong correlation with the lowest optical phonon modes at 180 cm^{-1} . Such experimental study establishes a relation between low-frequency dielectric function with the optical phonon mode for ferroelectric materials.

The theoretical investigation²⁻⁶ on TiO_6^{8-} unit of BaTiO_3 crystal predicted the origin of ferroelectric properties due to the PJT interaction among the electronic states ($^1A_{1g}$ and $^1T_{1u}$) through the t_{1u} modes, where the experimental studies¹⁴⁻¹⁹ on Raman active modes, dielectric optical properties and in particular, terahertz spectroscopy of powdered BaTiO_3 depicted strong electron-nuclear correlations leading to such ferroelectric material. In this context, we perform *ab initio* (MRCI) calculation to generate adiabatic potential energy surfaces (PESs) and non-adiabatic coupling terms (NACTs) of TiO_6^{8-} unit assuming the crystal structure of BaTiO_3 , where eight TiO_6^{8-} unit share one Barium (Ba) atom in an octahedral environment. Since the lowest four electronic states ($^1A_{1g}$ and $^1T_{1u}$) form the sub-Hilbert space²⁰ over the nuclear planes constituted with the normal modes (t_{1u} and t_{2g}), we employ Beyond Born-Oppenheimer (BBO) theory and construct the diabatic Hamiltonian for the system. Indeed, it is challenging issue due to the presence of d^0 transition metals, like Ti^{4+} possessing three state degeneracy, which would be the first time in literature.

The theoretical framework of Born-Oppenheimer (BO) treatment²¹ followed by Born and Huang²² approach can be considered as the starting point to study multi-mode multi-surface molecular pro-

cesses and chemical reactions. The two physically meaningful quantities, namely adiabatic potential energy surfaces (PESs) and non-adiabatic coupling terms (NACTs) are the major outcomes of the BO treatment, where both of them dictate the nuclear motion in physical-chemical processes. In other words, the eigenvalues of electronic Hamiltonian are known as adiabatic PESs on which the nuclei move and such movements of nuclei from one electronic state to another are due to the electron-nuclear couplings, also defined as the momentum couplings (NACTs) between different electronic states. On the contrary, when the interactions among the electronic states are neglected by imposing BO approximation for low energy processes, the dynamics of nuclei are presumably restricted on specific electronic states, but even for ground state, significant anomalies are observed between theoretically calculated and experimentally measured spectral profiles and/or scattering cross-sections obtained from multi-state molecular process or chemical reactions.²³⁻³⁰

Since the electron-nuclear couplings (NACTs) exhibit singular behaviour at and around the degenerate points (CIs) over the nuclear configuration space (CS) as depicted by Hellmann-Feynman theorem^{31,32}, a paradigm shift is required by transforming the adiabatic representation of Schrödinger equation (SE) to the diabatic framework, where those singular non-adiabatic (kinetic) couplings turn into well-behaved and smooth diabatic (potential) couplings. In the realm of diabatization schemes for realistic systems, a wide variety of approaches were introduced, namely, vibronic coupling model,³³⁻³⁶ exact factorisation scheme,^{37,38} direct dynamics approaches^{39,40} and many others^{26,41-45}. Nevertheless, the first principle (BBO) based adiabatic-to-diabatic transformation (ADT) formalism by F. T. Smith⁴⁶ for diatomic species followed by its non-trivial generalization by M. Baer⁴⁷⁻⁵¹ for triatomic chemical reactions as well as polyatomic molecular processes can be considered as the most “accurate” methodology for constructing diabatic Hamiltonian for a molecular system/chemical process. In the Baer’s formalism⁴⁷⁻⁴⁹, one needs to integrate a set of coupled differential (ADT) equations along two-dimensional contours over the interested domain of nuclear CS for a given sub-Hilbert space (SHS). If the initially chosen SHS forms a “true” sub-space, the “accuracy” of the diabatic PESs and couplings can be affirmed by exploring the validity of two important conditions, namely, (a) the mixing (ADT) angles along a loop enclosing n number of JT type CI(s) or RT interaction(s) or PJT coupling attain the integer (n) multiple of π or 2π or zero (0), respectively^{49,52,53}; and (b) the vector fields associated with the NACTs obey “Curl Condition”^{20,49,50}. On the other hand, later on, Adhikari and coworkers^{28,29,54-56} have developed

the first principle based BBO treatment for three to six state SHSs with an explicit formulation of NACTs as well as various ADT quantities (ADT equations, Curl-divergence equations and diabatic PESs matrix elements), which are being widely used for several realistic spectroscopically interesting molecules^{54,55,57-72}, solid state perovskites⁷³ as well as triatomic scattering processes^{65-67,74-78} to depict the workability of those ADT equations. In our recent works, we have generalized the BBO formalism by developing a user-friendly OpenMP parallelized program package, ‘ADT’⁵⁶ for symbolic formulation as well as numerical calculation of the ADT quantities (ADT angles, ADT matrices and diabatic PESs matrices) for any molecular system/chemical processes with N coupled electronic states and K number of nuclear degrees of freedom (DOFs).

The present article is organized as follows: Section 2 depicts the theoretical background of BBO theory as well as the working equations to compute the PE spectra and to explore the origin of ferroelectricity. On the other hand, Sections 3 and 4 demonstrate the details of *ab initio* calculations and functional forms of various *ab initio* quantities (adiabatic PESs and NACTs), respectively. The numerical results of various ADT quantities (ADT angles, ADT matrices and diabatic PESs matrices) are presented in Subsections 4.1 and 4.2. The TDDVR calculated PE spectra are depicted in Subsections 5.1 and the parametric dependence on ferroelectric properties are presented in Subsection 5.2. Finally, the conclusion of the entire work is laid down in Section 6.

2 Theoretical Background

2.1 Brief Outline of Beyond Born-Oppenheimer Theory

Since the molecular processes and chemical reactions are governed by the total electron-nuclear Hamiltonian, the associated molecular Schrödinger Equation (SE) takes the following form in terms of total Hamiltonian (\hat{H}) and wavefunction (Ψ):

$$\hat{H}(\mathbf{r}_e, \mathbf{R}_n)\Psi(\mathbf{r}_e, \mathbf{R}_n) = E\Psi(\mathbf{r}_e, \mathbf{R}_n), \quad (1)$$

where \mathbf{r}_e and \mathbf{R}_n signify electronic and nuclear coordinate vectors, respectively. For non-relativistic case, molecular Hamiltonian $\hat{H}(\mathbf{r}_e, \mathbf{R}_n)$ can be segregated into nuclear kinetic energy operator ($\hat{T}_{\text{nuc}}(\mathbf{R}_n)$) and electronic Hamiltonian ($\hat{H}_{\text{el}}(\mathbf{r}_e; \mathbf{R}_n)$) as follows:

$$\hat{H}(\mathbf{r}_e, \mathbf{R}_n) = \hat{T}_{\text{nuc}}(\mathbf{R}_n) + \hat{H}_{\text{el}}(\mathbf{r}_e; \mathbf{R}_n); \quad \hat{T}_{\text{nuc}} = -\frac{\hbar^2}{2}\nabla_R^2, \quad (2)$$

where $\nabla_{\mathbf{R}}$ symbolizes derivatives on mass-weighted nuclear coordinates (\mathbf{R}_n).

For a complete matrix (Hilbert) space of dimension M , total molecular wavefunction $[\Psi(\mathbf{r}_e, \mathbf{R}_n)]$ can be written as linear combination of electronic eigenfunctions ($\{\xi_i(\mathbf{r}_e; \mathbf{R}_n)\}$ s) through Born-Oppenheimer-Huang^{21,22} expansion:

$$\Psi(\mathbf{r}_e, \mathbf{R}_n) = \sum_{i=1}^M \psi_i^{\text{ad}}(\mathbf{R}_n) \xi_i(\mathbf{r}_e; \mathbf{R}_n), \quad (3)$$

where the combining coefficients are denoted as nuclear wavefunctions, $\{\psi_i^{\text{ad}}(\mathbf{R}_n)\}$. On the other hand, the electronic eigenfunctions ($\{\xi_i(\mathbf{r}_e; \mathbf{R}_n)\}$ s) are originated from the electronic SE:

$$\hat{H}_{\text{el}}(\mathbf{r}_e; \mathbf{R}_n) \xi_i(\mathbf{r}_e; \mathbf{R}_n) = u_i(\mathbf{R}_n) \xi_i(\mathbf{r}_e; \mathbf{R}_n), \quad \langle \xi_i | \xi_j \rangle_{\mathbf{r}_e} = \delta_{ij}, \quad (4)$$

where the eigenvalues, namely, adiabatic PESs ($\{u_i(\mathbf{R}_n)\}$ s) depend on nuclear coordinates. In Eq. 4, the expression $\langle \cdots \rangle_{\mathbf{r}_e}$ represents the inner product between two electronic eigenstates over electronic coordinates.

While substituting the BO expanded molecular wavefunction (Eq. 3), total Hamiltonian (Eq. 2) and electronic SE (Eq. 4) in the molecular SE (Eq. 1) and then, projecting with various electronic eigenfunctions, the kinetically coupled nuclear SE (known as adiabatic nuclear SE) takes the following form,

$$-\frac{\hbar^2}{2} (\nabla_{\mathbf{R}} + \boldsymbol{\tau})^2 \psi^{\text{ad}} + (U - E) \psi^{\text{ad}} = 0, \quad (5)$$

where the elements of diagonal adiabatic PESs matrix and skew-symmetric non-adiabatic coupling matrix $[\boldsymbol{\tau}_{ij}(\mathbf{R}_n) (= \langle \xi_i | \nabla_{\mathbf{R}} \xi_j \rangle_{\mathbf{r}_e})]$ can be written as:

$$U_{ij}(\mathbf{R}_n) = u_j(\mathbf{R}_n) \delta_{ij} \quad (6)$$

$$\langle \xi_j | \nabla_{\mathbf{R}} \xi_i \rangle_{\mathbf{r}_e} = -\langle \xi_i | \nabla_{\mathbf{R}} \xi_j \rangle_{\mathbf{r}_e} \quad (7)$$

If non-adiabatic matrix (τ) is dropped from Eq. 5, the coupling between electronic states will be absent, which is known as Born-Oppenheimer approximation. On the contrary, employing Hellmann-Feynman theorem,^{31,32} the electronic SE (Eq. 4) depicts that NACTs (see Eq. 7) encounter singularity at the close neighbourhood of degenerate point(s) over the nuclear configuration

space (CS):

$$\boldsymbol{\tau}_{ij} = \frac{\langle \xi_i | \nabla_R \hat{H}_{\text{el}} | \xi_j \rangle_{\mathbf{r}_e}}{u_j - u_i}. \quad (8)$$

Therefore, a paradigm shift from adiabatic to diabatic representation of nuclear SE is indeed necessary to wipe out the often singular kinetic (NACTs) couplings by well-behaved potential (diabatic) couplings to avoid the numerical inaccuracies that could arise in dynamical calculations with adiabatic SE. Such changeover (adiabatic to diabatic) is carried out using the transformation $\psi^{\text{ad}} = A\psi^{\text{dia}}$, where ψ^{ad} and ψ^{dia} represent adiabatic and diabatic basis, respectively. After substituting such relationship ($\psi^{\text{ad}} = A\psi^{\text{dia}}$) in Eq. 5, one can achieve the following diabatic representation of nuclear SE:

$$\left(-\frac{\hbar^2}{2} \nabla_R^2 + W - E \right) \psi^{\text{dia}} = 0, \quad W = A^\dagger U A, \quad (9)$$

under the Adiabatic-to-Diabatic Transformation (ADT) condition:⁴⁹

$$\nabla_R A + \boldsymbol{\tau} A = 0. \quad (10)$$

Since $\boldsymbol{\tau}$ matrix for M dimensional Hilbert space is skew-symmetric in nature, the above-mentioned ADT condition affirms the orthogonal property of A matrix [$SO(M)$]. The generalized form of A matrix is depicted elsewhere^{66,70}.

While substituting the generalized form of ADT (A) and the skew-symmetric $\boldsymbol{\tau}$ matrix in ADT condition (Eq. 10), we obtain ${}^N C_2 (= P)$ number of first order differential equations as follows:

$$\nabla_R \Theta_{ij} = \sum_{m=1}^P c^{(m)} \boldsymbol{\tau}^{(m)}, \quad (11)$$

where $\boldsymbol{\tau}^{(m)}$ signify NACTs between different electronic states and the associated coefficients, $\{c^{(m)}\}$ s appear as trigonometric functions of ADT angles $\{\Theta_{kl}\}$ (see Section S3 of the Electronic Supplementary Information (ESI)). Employing a package program⁵⁶, the details of such formulation of differential equation for any chemical or physical process involving N electronic states and M vibrational modes can be obtained through symbolic manipulation, where the numerical solution of ADT angles ($\{\Theta_{ij}\}$) using *ab initio* calculated NACTs could be carried out.

2.1.1 Conditions for the Existence of Sub-Hilbert Space

While transforming the adiabatic SE (Eq. 5) to Diabatic one (Eq. 9), it is necessary to satisfied ADT equation (see Eq. 10). Since ADT is a set of differential equation involved with vector fields, $\boldsymbol{\tau}$

and those fields could often be singular (see Eq. 8) in the nuclear CS, such molecular fields have to keep the conservation of energy for a chosen SHS associated with a molecular process or a chemical reaction. In other words, with the cross derivatives on the scalar components of ADT equation lead to the ADT condition that has one to one correspondence with the curl condition of a vector field as appears in classical electrodynamics (for more details, see Section S2 of the ESI). If such condition is satisfied for a chemical or physical process involving certain number of electronic states, we may safely predict that those states form a SHS over interested energy domain. Moreover, as the NACTs (τ) could be singular (see Eq. 8), those terms will depict an integer multiple of π on contour integration like any other singular function, if the *ab initio* NACTs (τ) are calculated with appropriately defined sub-Hilbert space.

For a sub-Hilbert space, the NACT components should obey the following conditions for two-dimensional (p - q) cross-section of M dimensional nuclear degrees of freedom (DOFs):

(a) Cauchy’s residue theorem: Quantization of NACTs over the polar counterpart, $\rho - \phi$:

$$\int_0^{2\pi} \tau_{ij}^\phi(\rho_0, \phi) d\phi = 0 \text{ or } n\pi \text{ or } n \cdot 2\pi, \quad (12)$$

validates the presence of PJT interactions or n number of JT or RT interactions, respectively, encapsulated by the closed contour of integration, where $\tau_{ij}^\phi(\rho_0, \phi)$ represents angular (ϕ) component of NACT between $\{i, j\}$ electronic states along the angular coordinate ϕ at $\rho = \rho_0$.

(b) When we take cross derivatives on the scalar components of ADT conditions (Eq. 10), the Curl conditions appear as:

$$\frac{\partial}{\partial p} \tau_{ij}^q - \frac{\partial}{\partial q} \tau_{ij}^p = (\tau^q \tau^p)_{ij} - (\tau^p \tau^q)_{ij}, \quad (13)$$

which needs to be fulfilled by the p and q components of NACTs and the associated matrix elements

$$F_{ij}^{pq} = \left[\frac{\partial}{\partial p} \tau_{ij}^q - \frac{\partial}{\partial q} \tau_{ij}^p \right] - \left[(\tau^q \tau^p)_{ij} - (\tau^p \tau^q)_{ij} \right] = Z_{ij}^{pq} - C_{ij}^{pq}, \quad (14)$$

should acquire the magnitude of zero (0).

Even though, in principle, the above two conditions are valid for a complete Hilbert space, it is important to explore the existence of a sub-Hilbert space for all “practical” purposes (of computation) and to construct finite $[N (<< M)]$ dimensional “accurate” diabatic Hamiltonian matrix. In other words, for an initially chosen sub-Hilbert space (SHS), if the above conditions (Eqs. 12 and

S15) are not fulfilled, the sub-space needs to be expanded to achieve desired level of accuracy in the diabatic Hamiltonian so that the non-removable component of NACTs becomes negligible and the removable part can be “truly” diabaticized.

2.1.2 Path Dependence of ADT vis-à-vis Diabatic PES Matrices

Since the BBO theory involves skew-symmetric non-Abelian non-adiabatic coupling matrix (NACM) for three or higher dimensional sub-Hilbert space, the solution of ADT (coupled differential) equations can be path dependent with the choice of contour over the two-dimensional cross-sections of multi-dimensional space of nuclear degrees of freedom. For p - q nuclear plane, if the integral forms of the orthogonal ADT matrices for two different paths with same final nuclear configuration are represented by A_1 and A_2 ⁵⁷, the associated diabatic PESs matrices ending at same point can be represented as:

$$W_1 = A_1^\dagger U A_1 \quad \text{and} \quad W_2 = A_2^\dagger U A_2, \quad (15)$$

which leads to

$$A_1 W_1 A_1^\dagger = A_2 W_2 A_2^\dagger = U \quad (16)$$

arriving at

$$W_1 = B W_2 B^\dagger. \quad (17)$$

Since A_1 and A_2 are orthogonal transformation matrices, the product $B (= A_1^\dagger A_2)$ also appears as an orthogonal matrix ($B^\dagger B = A_2^\dagger A_1 A_1^\dagger A_2 = I$) and therefore, the Eq. 17 ensures the path independence of the calculated observables originated from different diabatic PESs matrices (W_1 and W_2).^{57,67,68,72}

2.2 Calculation of Photoemission Spectra

Once the BBO based diabatic PESs and couplings of the titled system (TiO_6^{8-}) are in hand, we carry out multi-state multi-mode Time-Dependent Discrete Variable Representation (TDDVR) dynamics^{73,79–83} (see Section S10 of the ESI) to calculate the photoemission (PE) spectra of TiO_6^{9-} moiety. While solving the TDSE during dynamical calculations, the nuclear wavefunctions at different time

are employed to compute the autocorrelation function ($C(t)$):

$$C(t) = \langle \Xi(t) | \Xi(0) \rangle \quad (18a)$$

$$= \left\langle \Xi^* \left(\frac{t}{2} \right) \middle| \Xi \left(\frac{t}{2} \right) \right\rangle. \quad (18b)$$

It is worth mentioning that the second expression (Eq. 18b) is more accurate and computationally less expensive compared to the first one (Eq. 18a), but it (Eq. 18b) can only be used for real initial wavefunction and totally symmetric (A_1) Hamiltonian. The calculated autocorrelation functions are further used to generate the spectral intensity at peak positions with the help of the following Fourier Transformation:

$$I(\omega) \propto \omega \int_{-\infty}^{\infty} C(t) \exp(i\omega t) dt, \quad (19)$$

where the integration time limit is taken as 0 to 100 fs for our present calculation.

Since the resolution of the spectrometer results into phenomenological broadening in the experimental spectral lines, the theoretical autocorrelation function needs to be multiplied with a damping time-dependent function:

$$h(t) = \exp \left[- \left(\frac{|t|}{\tau} \right)^2 \right] \quad (20)$$

where the unit of τ is considered as 10^{-14} sec. Furthermore, while calculating the propagation of the wavefunction and the autocorrelation function within a finite time frame, artifacts known as the Gibbs phenomenon can arise in the spectrum. These artifacts can be reduced by multiplying the autocorrelation with the following function,

$$g(t) = \cos^n \left(\frac{\pi t}{2T} \right), \quad (21)$$

where n is an integer number set to 2 in this context and T denotes the length of propagation. Readers are requested to go through earlier articles^{69,82,83} to acquire in-depth knowledge about the calculation of theoretical spectra by TDDVR formalism.

2.3 Calculation of Ferroelectricity

In case of TiO_6^{8-} unit of BaTiO_3 crystal, we will utilize presently calculated *ab initio* adiabatic PESs to analyze the structural distortion, employing an equation derived from the mean-field Hamiltonian,

$H = H_0 - \lambda Q \langle Q \rangle$. This equation incorporates the potential energy, $U = U_0 - \lambda Q \langle Q \rangle$, where $\langle Q \rangle$ is a parameter leading to a system of coupled transcendental equations⁸⁴:

$$\langle Q_j \rangle = \frac{\int Q_j \exp^{-U(Q)/kT} d^3Q}{Z}, \quad Z = \int \exp^{-U(Q)/kT} d^3Q, \quad (22)$$

where j represents one of the any axis (x or y or z) of distortion. Since this phase transition occurs due to the change of geometry from tetragonal to cubic or the reverse, one can consider that the titanium ion (Ti^{4+}) undergoes displacement along a specific direction, let say, the z -axis. Therefore, assuming zero displacements along the x and y axes ($Q_x = Q_y = 0$), the partition function for the displacement along the z -axis can be expressed as:

$$\langle Q_z \rangle = \frac{\int Q_z \exp^{-U(Q_z)/kT} dQ_z}{Z}, \quad Z = \int \exp^{-U(Q_z)/kT} dQ_z. \quad (23)$$

This framework is used to calculate the ferroelectric properties based on the structural distortions.

3 Details of *Ab Initio* calculation on TiO_6^{8-} moiety

In the present work, first we compute the vibrational frequencies of TiO_6^{8-} unit of $BaTiO_3$ cluster with the aid of Coupled-Cluster with Singles and Doubles (CCSD) method employing atomic natural orbital (ANO-R1) basis set as implemented in MOLPRO quantum chemistry software⁸⁵ and compare those with the existing theoretical data^{5,86} (see Table I). On the other hand, within the Franck-Condon (FC) domain of nuclear CS, the adiabatic PESs are calculated using Complete Active Space Self-Consistent Field (CASSCF) followed by Multi-Reference Configuration Interaction (MRCI) approach, where NACTs are evaluated by CASSCF based Numerical Finite Difference (DDR) methodology. Since the degeneracies of the valence molecular orbitals (t_{1u}) as well as all other inner-shell orbitals are perfectly reproduced while taking all the six $Ti - O$ bonds equal with length of 2.0 Å, such undistorted geometry is considered as the origin of the nuclear CS. Moreover, such choice of bond length (2.0 Å) is in conformity both with experimental finding⁸⁷ and other theoretical prediction⁸⁸. It is worth mentioning that the entire calculation is performed using six (6) electrons in six (6) orbitals forming complete active space (CAS) involving filled HOMO (t_{1u}) and virtual LUMO (t_{2g}^*) orbitals leading to the correct order of energies for the ground ($^1A_{1g}$) and excited ($^1T_{1u}$) electronic states as well as degeneracies in the excited ($^1T_{1u}$) electronic states for the

undistorted geometry ($Ti - O$ bond length = 2.0 Å).

Since the ground and first three excited states belong to A_{1g} and T_{1u} symmetry, respectively, the symmetry driven condition depicts that the g symmetric triply degenerate normal modes (t_{2g} , frequency = 266.81 cm^{-1}) lead to JT distortion for the T_{1u} symmetric excited electronic states, whereas PJT couplings are observed between A_{1g} and T_{1u} states along t_{1u} normal modes (frequency = 123.87 cm^{-1}). The detailed conditions for the JT and PJT interactions between various electronic states and normal modes are analysed in Section S1 of the ESI. In our calculation, all the six normal modes (three t_{1u} and three t_{2g} symmetric) are included to construct six two-dimensional (2D) nuclear planes, namely $Q_{t_{1ux}} - Q_{t_{1uy}}$, $Q_{t_{1uy}} - Q_{t_{1uz}}$, $Q_{t_{1uz}} - Q_{t_{1ux}}$, $Q_{t_{2gx}} - Q_{t_{2gy}}$, $Q_{t_{2gy}} - Q_{t_{2gz}}$ and $Q_{t_{2gz}} - Q_{t_{2gx}}$ to compute the adiabatic PESs and NACTs followed by construction of diabatic Hamiltonian (PESs and couplings). We explore the contribution of both types of non-adiabatic couplings, namely, JT interactions in excited states and PJT stabilization of ground state, and finally, in the diabatic Hamiltonian through the photoemission (PE) spectra. Moreover, we also execute *ab initio* calculations of the 2D cross-section for the nuclear plane, $Q_{t_{1ux}} - Q_{t_{1uy}}$ for various values of $Q_{t_{1uz}}$ normal mode and obtain a global minima, where the corresponding bond lengths are presented in Table I along with other results obtained from Green's function DFT calculations⁵. It may be noted that Green's function DFT⁵ calculations is based on single-reference, whereas we performed multi-reference (MRCI-SD) calculation and thereby, the accuracy of our calculation is much higher.

4 *Ab Initio* and ADT Quantities

Since we intend to acquire the structural insights of TiO_6^{8-} unit of BaTiO_3 crystal, the inherent non-adiabatic interactions (JT/accidental CIs and PJT couplings) over six chosen normal mode pairs are explored. In order to investigate the validity of quantization of NACTs along a closed path over the 2D nuclear planes, mass-weighted normal mode coordinates are converted into their polar analogues as depicted below:

$$Q_k = \rho \cos \phi \quad \text{and} \quad Q_l = \rho \sin \phi,$$

where Q_k, Q_l are any two components of t_{1u} or t_{2g} symmetric normal modes, and ρ and ϕ symbolize their polar counterpart. For better identification, the lowest four electronic states are numbered

TABLE I: Comparison of various molecular parameters between presently calculated and other theoretical results, where Q_0 represents the saddle point, K_0 is the force constant for the Q displacement and global minimum point, $\{Q_{t_{1ux}}^{gm}, Q_{t_{1uy}}^{gm}, Q_{t_{1uz}}^{gm}\}$.

Parameters	CCSD	Green's Function DFT ⁵
$\hbar w_e(t_{1u})(cm^{-1})$	123.87	193 (also Ref. 86)
$\hbar w_e(t_{2g})(cm^{-1})$	266.81	—
	MRCI(SD)	
$Q_{t_{1ux}}^{gm} = Q_{t_{1uy}}^{gm} = Q_{t_{1uz}}^{gm} (\text{\AA})$	0.51	0.14
$Q_o (\text{\AA})$	0.64	0.16
$K_o (eV/\text{\AA})$	44.18	55
$E_{PJT} (eV)$	2.582	4.0
$E_{JT} (eV)$	0.0182	—

as per the increasing order of energy: $^1A_{1g} \rightarrow 1$ and $^1T_{1u} \rightarrow 2 - 4$. For each 2D nuclear plane ($\rho - \phi$), we have considered 70×181 *ab initio* grid points, where the ρ and ϕ coordinates span from 0.2 to 14.0 and 0 to 2π , respectively. In other words, the normal modes ($\{Q_i\}$) range from -1.5 Å to 1.5 Å, which encapsulate the entire FC domain of nuclear CS. Since the displacements along all the three components (x, y or z) of t_{1u} or t_{2g} symmetric normal modes lead to identical geometries, the adiabatic potential energy curves (PECs) and NACTs are superimposable with each other (see in Figures 1 and S1 of the ESI). One can find repetition of those profiles every after 90° in the polar forms of the normal modes, $Q_x = \rho \cos\phi$ and $Q_y = \rho \sin\phi$ ($0 \leq \phi < 2\pi$), which is the inherent symmetry of the molecular species. Therefore, the detailed discussion on adiabatic PESs, NACTs, ADT angles, ADT matrices and diabatic PESs matrices are presented below only for two representative planes, $Q_{t_{2gx}} - Q_{t_{2gy}}$ and $Q_{t_{1ux}} - Q_{t_{1uy}}$ belonging to two different symmetries.

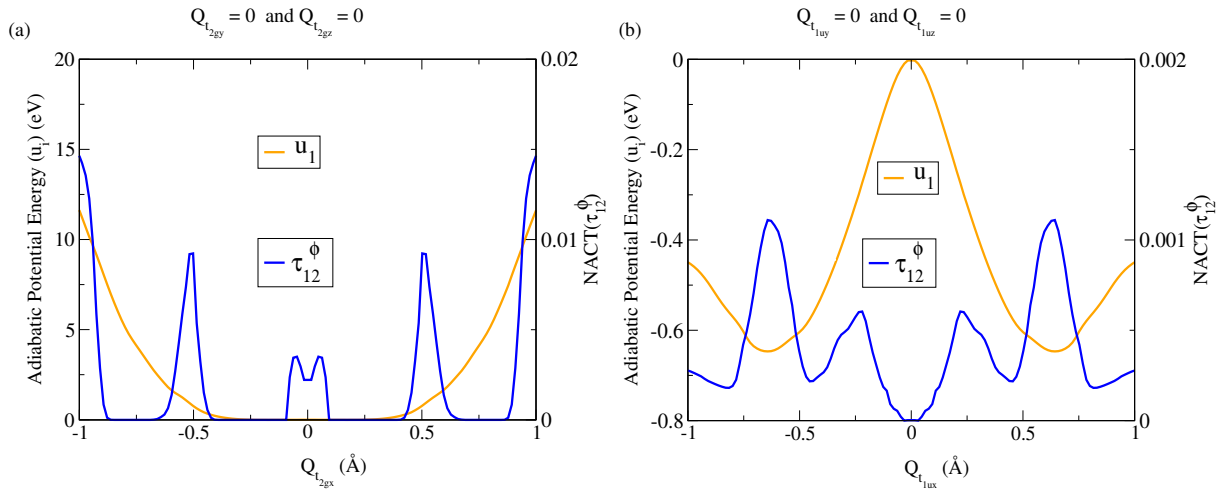


Fig. 1: For TiO_6^{8-} unit, 1D curves of lowest adiabatic PES (u_1) and the associated NACT (τ_{12}^ϕ) are presented along (a) $Q_{t_{2gx}}$ and (b) $Q_{t_{1ux}}$ normal modes keeping the other normal modes fixed at zero (0).

4.1 $Q_{t_{2gx}} - Q_{t_{2gy}}$ Pair

The one-dimensional (1D) functional forms of adiabatic PESs (scaled with respect to the excited state energy at $\{Q_0\}=0$) and NACTs for three excited electronic states ($^1T_{1u}$) are presented along $Q_{t_{2gx}}$ normal modes in Figure 2, which clearly shows a three point (“2-3-4”) JT CI at the origin ($\{Q_{t_{2gx}}, Q_{t_{2gy}}$ and $Q_{t_{2gz}}\} = 0$). On the other hand, two (2) additional “2-3” accidental CIs are observed along each normal mode $Q_{t_{2gx}} = 0.14 \text{ \AA}$ at $Q_{t_{2gy}} = 0$ leading to total four (4) “2-3” CIs over $Q_{t_{2gx}} - Q_{t_{2gy}}$ plane. Further details, including calculation of local topographic parameters and model double-cone adiabatic PESs around the “2-3” CI, are provided in Section S5 of the ESI. These results confirm that the degeneracy is lifted linearly, consistent with the conical nature of the intersections. Even though $Q_{t_{2g}}$ is JT active mode for $^1T_{1u}$ symmetric electronic states, the magnitude of JT stabilization energy appears as very low (0.0182 eV). The 2D functional features of ϕ components of NACTs associated with JT and accidental CIs (τ_{23}^ϕ and τ_{34}^ϕ) are presented over $Q_{t_{2gx}} - Q_{t_{2gy}}$ plane in Figures 3(a-b). In case of “2-3” interactions, singularities of NACTs for all the four accidental CI points coalesce to one connecting seam passing through the origin, whereas τ_{34}^ϕ exhibits singularity only at the “2-3-4” JT CI point. On the other hand, PJT couplings are observed between A_{1g} and T_{1u} electronic states (“1-2”, “1-3” and “1-4”) among which τ_{12}^ϕ and τ_{14}^ϕ are displayed in Figures 3(c-d) to depict their well-behaved functional forms over the chosen domain of nuclear CS.

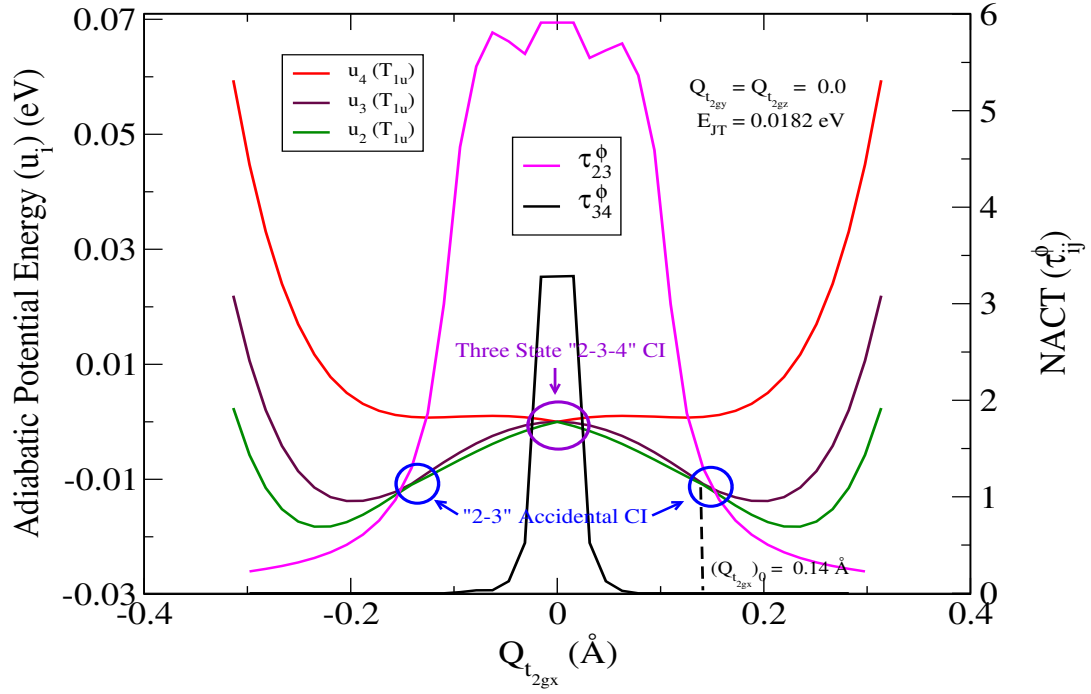
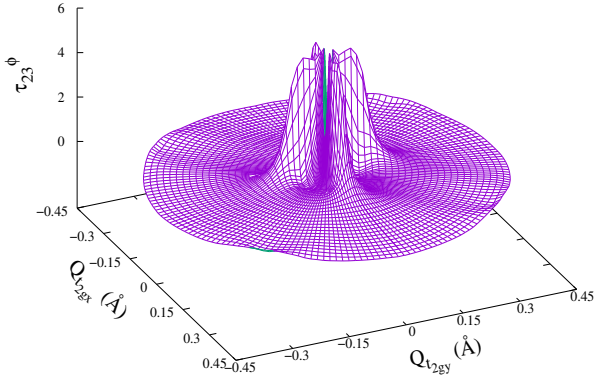
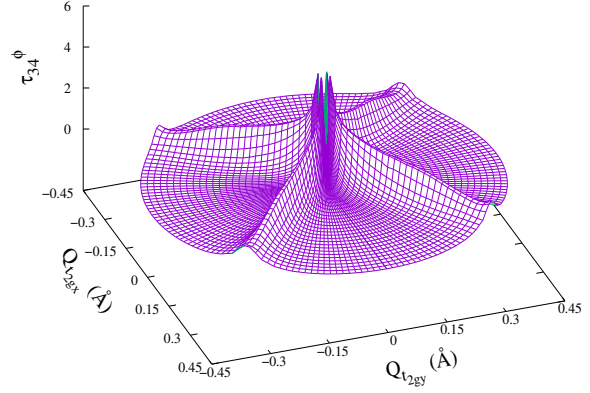


Fig. 2: For TiO_6^{8-} unit, 1D cuts of adiabatic PESs (u_2 , u_3 and u_4) and NACTs (τ_{23}^ϕ and τ_{34}^ϕ) for three excited electronic states (T_{1u}) are shown along $Q_{t_{2gx}}$ normal modes keeping the other t_{2g} coordinates fixed at zero (0). Similarly, the 1D cuts of adiabatic PESs and NACTs as functions of $Q_{t_{2gy}}$ or $Q_{t_{2gz}}$ will be exactly same.

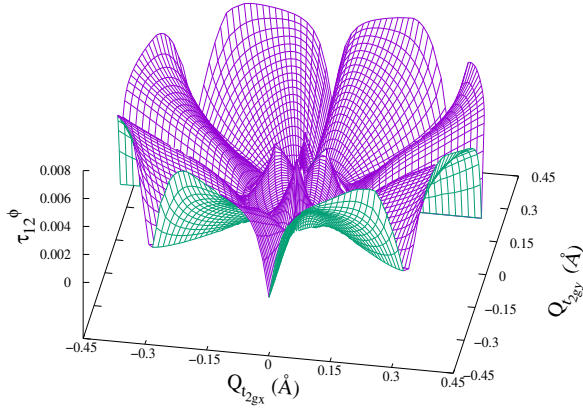
(a)



(b)



(c)



(d)

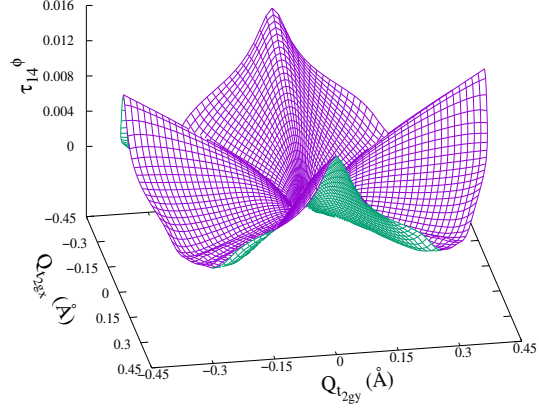


Fig. 3: Variation of ϕ component of NACTs, namely, (a) τ_{23}^ϕ , (b) τ_{34}^ϕ , (c) τ_{12}^ϕ and (d) τ_{14}^ϕ are plotted over $Q_{t_{2gx}} - Q_{t_{2gy}}$ plane. The functional forms of NACT for four “2-3” accidental CIs and one three state (“2-3-4”) JT CIs show coalesce of each type CIs at the centre of t_{2g} coordinates.

As per Cauchy’s residue theorem (see Eq. 12), if a closed contour of integration encloses PJT interaction(s) or JT or RT CI(s)/seam(s), the resulting ADT angles attain the magnitude of zero (0) or integer (n) multiple of π or 2π and the associated diagonal elements of ADT matrices undergo n number of sign inversions. The calculation of ADT angles employing the ADT equation, $\nabla A + \tau A = 0$, are carried out using the *ab initio* calculated NACM (τ) and thereby, there is no control on the nature of the profiles (see Eqs. 10 and 11). In fact, within numerical accuracy, one can say ADT angles are “*ab initio*” calculated and their functional nature could be linear or non-linear, but at the end of the closed contour, those angles attain 0, $n\pi$ and $n \cdot 2\pi$ depending upon the nature of the interaction, PJT, JT and RT, respectively. The geometric phase is linearly dependent on the circular coordinate (ϕ), where the ADT angles could vary non-linearly as a function of such coordinates (ϕ). On the other hand, while constructing the diabatic PESs and couplings, we solve the ADT equation along any chosen path and thereby, that is no unique diabatic matrix, but those matrices (due to different paths) are related through the orthogonal transformation providing unique observables^{57,67,68} (see Subsection 2.1.2). On the contrary, while locating the CIs and their nature (PJT, JT and RT), we need to solve ADT equation along a circular coordinate (ϕ) fixing the other coordinates at specific value and thereby, the functional form of ADT angle along such path will be specific for each different CIs. In the present work, diabaticization is carried out using two state as well as four state ADT equations, where the quantization of NACTs is affirmed for both the cases. In case of $Q_{t_{2gx}} - Q_{t_{2gy}}$ pair, Figure 4 depicts 1D variation of ADT angles (Θ_{23} and Θ_{34}) along ϕ coordinate for specific values of ρ , which attain the magnitude of π for two and four states. It is worth mentioning that the ADT angles appear as non-linear complicated functions of ϕ , which differ from two to four state calculation even for a specific molecular process indicating four state sub-Hilbert space. The non-linear functional form of each ADT angle leads to the associated phase ($\omega_\phi(\phi)$) topological ($e^{\pm i\omega_\phi(\phi)}$) in nature instead of geometric ($e^{\pm i\frac{n\phi}{2}}$, n is the number of enclosed CI(s)/seam(s))⁸⁹⁻⁹¹.

Once the ADT angles are in hand, we employ those four state ADT angles in the explicit expressions of NACTs (see Section S3.2 of the ESI) to recalculate those quantities to evaluate Mathematical Curls ($Z_{ij}^{\rho\phi}$) and ADT Curls ($C_{ij}^{\rho\phi}$).²⁰ Figure 5 shows that the $Z_{23}^{\rho\phi}$ and $C_{23}^{\rho\phi}$ (which incorporates “2-3” accidental JT CIs) as well as $Z_{34}^{\rho\phi}$ and $C_{34}^{\rho\phi}$ (which accommodates symmetry driven “3-4” JT CI) are almost superimposed with each other and therefore, the resulting matrix elements of Curl

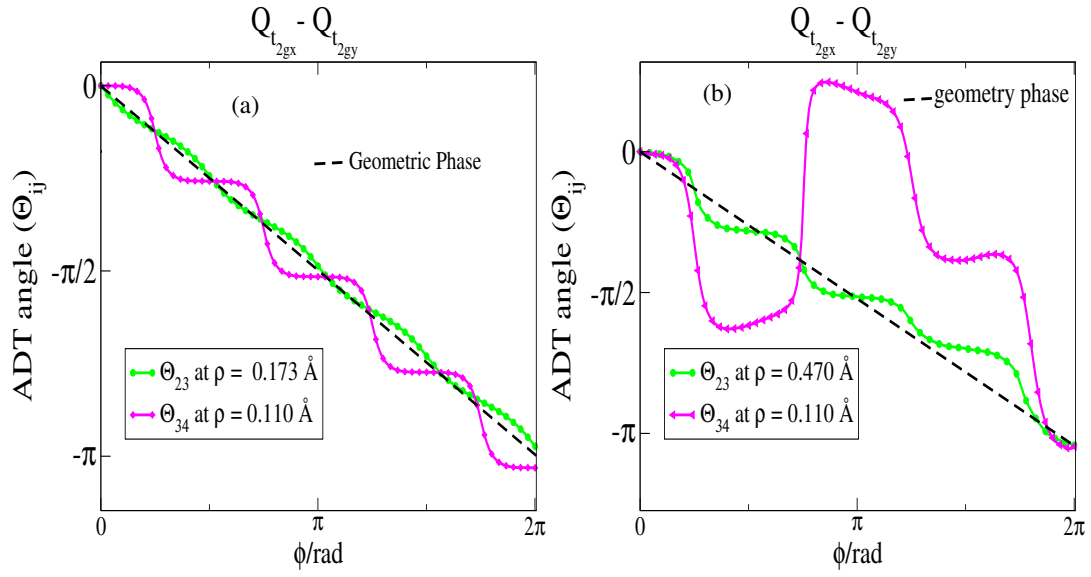


Fig. 4: 1D cuts of ADT angles for $Q_{t_{2gx}} - Q_{t_{2gy}}$ pairs, namely, Θ_{23} and Θ_{34} originated from (a) two and (b) four state ADT calculations are presented along the angular coordinate, ϕ for specific values of ρ , which attain the magnitude of π at the end of the contour.

Condition ($F_{23}^{\rho\phi}$ and $F_{34}^{\rho\phi}$) appear close to zero ($< 10^{-15} \text{ \AA}^{-2}$). In other words, those four electronic states ($^1A_{1g}$, $^1T_{1u}$) of TiO_6^{8-} unit form a subspace.

While computing the diabatic Hamiltonian over 2D nuclear planes, the ADT equations are first integrated along ϕ coordinate from 0 to 2π at a fixed magnitude of ρ ($= \rho_{min}$) and then, along ρ coordinate for each ϕ value (Path II, see Section S9 of the ESI). Once we obtain the ADT angles vis-à-vis ADT matrices, the similarity transformation (see Eq. 9) is carried out to obtain the diabatic PESs matrices. Figure 6 displays some representative diabatic PESs (W_{22} and W_{33}) and coupling (W_{23}) over the $Q_{t_{2gx}} - Q_{t_{2gy}}$ plane. It is interesting to note that the diabatic PESs and couplings exhibit a four-fold symmetry over the nuclear plane, since nuclear displacements along each of the normal modes, $Q_{t_{2gx}}$ and $Q_{t_{2gy}}$ lead to equivalent geometry as depicted in Figures 1 and S1 of the ESI. Such diagrams clearly depict smooth, continuous and single-valued forms of diabatic PES matrix elements at each and every grid point over the nuclear CSs, which validates the workability of our first principle based BBO formalism for a transition metal complex (solid state perovskite) possessing four electronic state sub-Hilbert space.

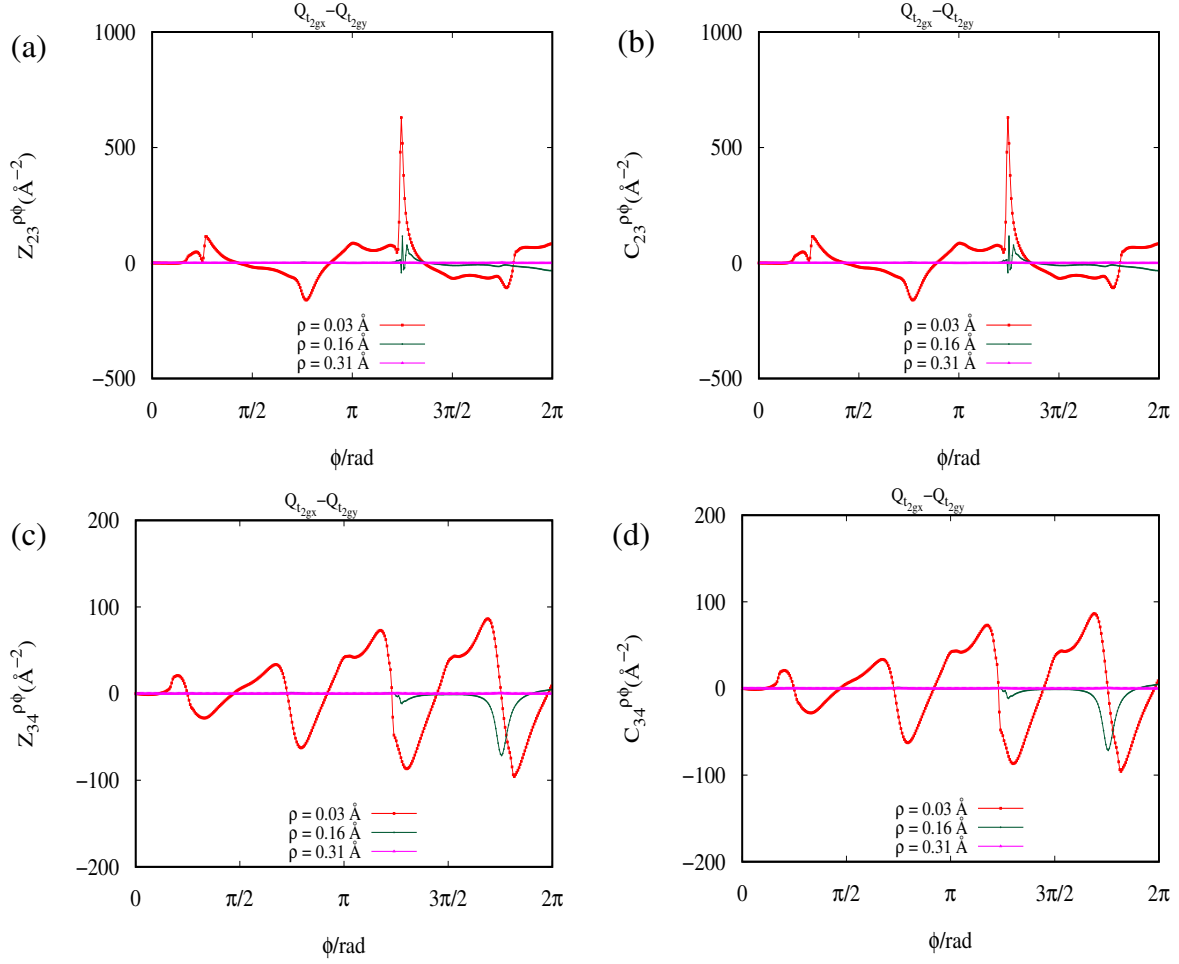


Fig. 5: The left and right panels depict Mathematical Curls [(a) $Z_{23}^{\rho\phi}$ and (c) $Z_{34}^{\rho\phi}$] and ADT Curls [(b) $C_{23}^{\rho\phi}$ and (d) $C_{34}^{\rho\phi}$] along the angular coordinate (ϕ) at three different ρ values for $Q_{t2gx} - Q_{t2gy}$ plane of TiO_6^{8-} unit of BaTiO_3 crystal.

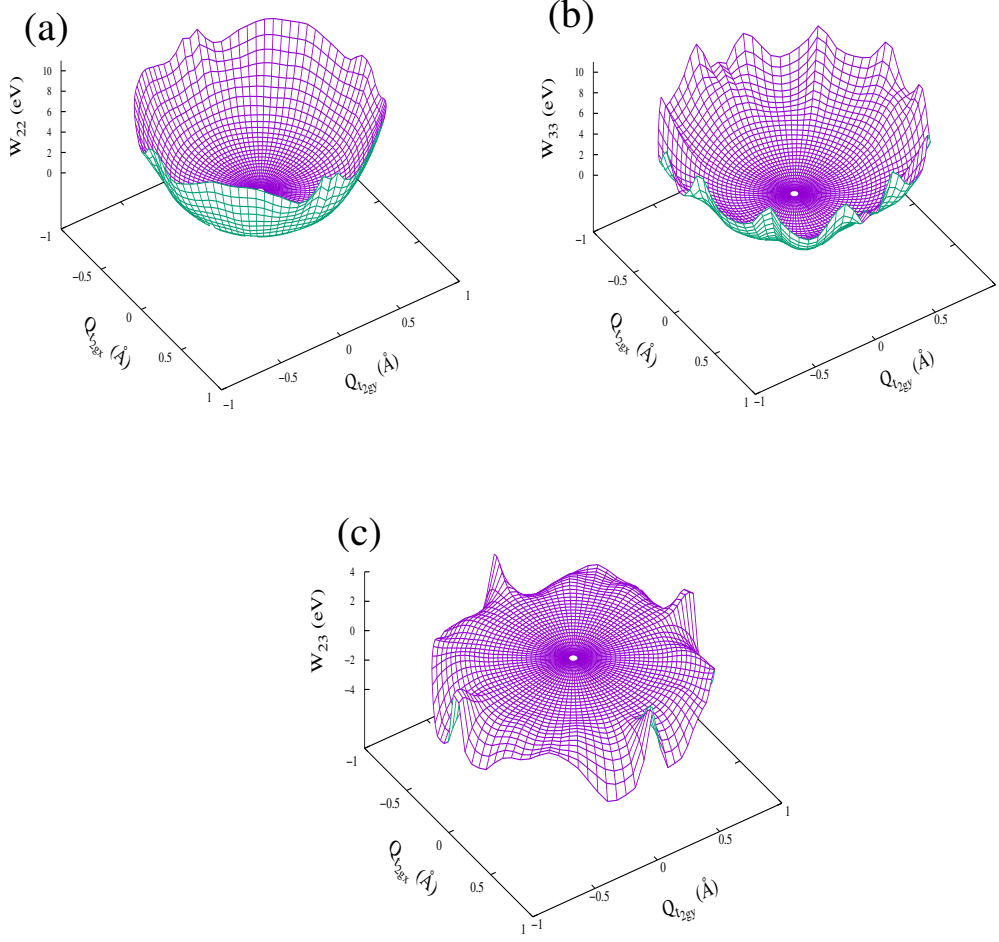


Fig. 6: 2D functional forms of diabatic surfaces for $Q_{t2gx} - Q_{t2gy}$ plane of TiO_6^{8-} unit of BaTiO_3 crystal, namely, (a) W_{22} and (b) W_{33} , and the associated diabatic coupling, (c) W_{23} are presented, where all the quantities appear as well-behaved functions of nuclear coordinates.

4.2 $Q_{t_{1ux}} - Q_{t_{1uy}}$ Pair

The u -symmetric normal mode pairs, namely, $Q_{t_{1ux}} - Q_{t_{1uy}}$ are mainly responsible for profound PJT interactions between ground (A_{1g}) and first excited (T_{1u}) electronic states. The 1D curves of the four adiabatic PESs (u_1 , u_2 , u_3 and u_4) are presented in Figure 7 along $Q_{t_{1ux}}$ and $Q_{t_{1uy}}$ normal modes indicating the presence of minima around $Q_{t_{1ux}} = \sim 0.944$ Å or $Q_{t_{1uy}} = \sim 0.944$ Å. In case of first three excited states, the degeneracies remain almost intact throughout the 1D curve due to absence of any JT distortion.

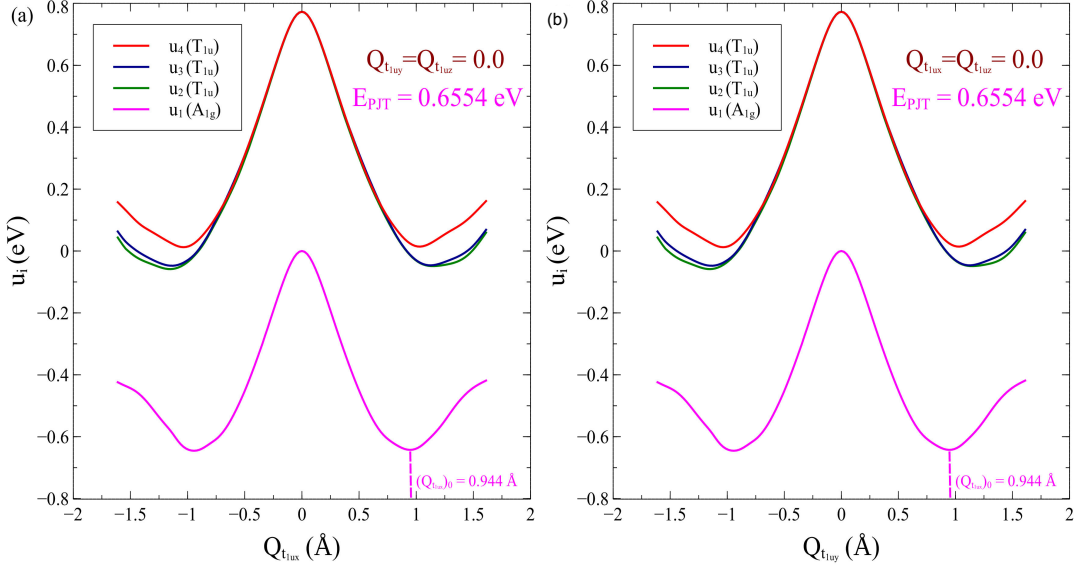


Fig. 7: 1D curves of adiabatic PESs for ground (A_{1g}) and first three excited electronic states (T_{1u}) are presented along (a) $Q_{t_{1ux}}$ and (b) $Q_{t_{1uy}}$ normal mode keeping the other t_{1u} coordinates ((a) $Q_{t_{1uy}}$ or (b) $Q_{t_{1ux}}$ and $Q_{t_{1uz}}$) fixed at zero (0).

On the other hand, Figure 8 depicts the 2D PESs over $Q_{t_{1ux}} - Q_{t_{1uy}}$ plane, which leads to four equivalent elongated octahedron structure (all the four positive and negative combinations, $Q_{t_{1ux}} = Q_{t_{1uy}} = \pm 0.86$ Å) with high stabilization energy (~ 1.578 eV). On the other hand, if all the three normal modes vary simultaneously, one can find eight global minima appearing at $Q_{t_{1ux}} = Q_{t_{1uy}} = Q_{t_{1uz}} = \pm 0.51$ Å stabilized by 2.582 eV, which differs substantially from predicted value (~ 4 eV) by Green's function DFT methodology⁵. The accuracy of present calculation for PJT stabilization energy is validated through the following investigations.

In Figure S4 of the ESI, we depict the triply degenerate (t_{1u}) bending modes, where Figure S5 of the ESI displays the initial as well as optimized geometries. The Figure S6 of the ESI shows the PJT

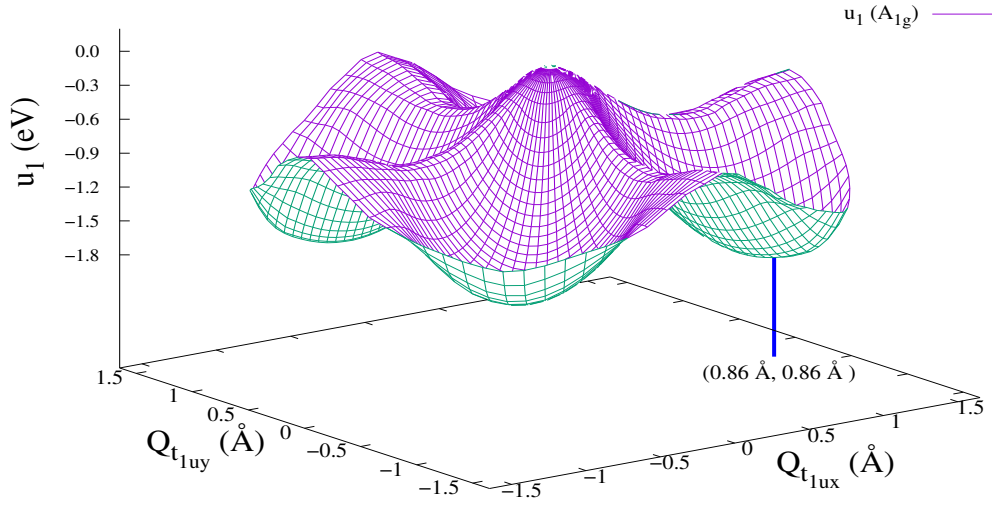


Fig. 8: 2D functional form of the ground adiabatic surface, u_1 is presented over the $Q_{t1ux} - Q_{t1uy}$ plane, where the nuclear configuration of PJT distorted minima is shown at $Q_{t1ux} = Q_{t1uy} = 0.86 \text{ Å}$.

stabilized ground state (A_{1g}) in which the $Ti - O$ bond lengths along the $\{x-y\}$ and z directions are 2.07 Å and 2.0 Å, respectively and the bond angles are close to 104° and 75° . To verify such structure, we have carried out geometry optimization calculations using relaxed scans at the SA-4-CAS (6o,6e)/ANO-R1 level of theory, followed by a single-point MRCI energy calculation. On the process of performing such optimization, the initial guess geometry has been taken as $\{Q = 0\}$, which represents a perfect octahedron configuration with $Ti - O$ bond length, 2.0 Å. In Figure S5 of the ESI, the optimized geometry displays elongated $Ti - O$ bond length, 2.07 Å, along the $\{x-y\}$ direction, but the length along the z -direction remains same, 2.0 Å. Moreover, the bond angles are very close to 90° . It is worth noting that any other initial guess geometries (including elongated octahedron structure) also lead to the same optimized structure. In other words, the ground state minimum energy structure obtained by scanning along the t_{1u} mode closely matches the optimized structure from the relaxed scan. Furthermore, Figure 8 shows that the PJT stabilization energy of the optimized structure is 1.5 eV, which coincides with the stabilization energy obtained from a 2D scan over the t_{1u} normal mode pair. Since the u -symmetric normal modes result into only PJT couplings (no JT interaction) within the low-lying four electronic states of TiO_6^{8-} unit, the 2D functional forms of ϕ components of NACTs representing (a) “1-2” (τ_{12}^ϕ), (b) “1-3” (τ_{13}^ϕ) and (c) “1-4” (τ_{14}^ϕ) PJT interactions are depicted in Figure 9, which naturally devoid of any singularity.

As depicted by Cauchy’s residue theorem (see Eq. 12), if a closed contour encapsulates PJT interaction(s), the calculated ADT angles acquire the value of zero (0) and therefore, the corresponding diagonal elements of ADT matrices do not undergo any sign inversion. Figure 10 depicts 1D functional forms of three ADT angles, namely, Θ_{12} , Θ_{13} and Θ_{14} along the ϕ coordinates at specific fixed values of ρ . It is interesting to observe that the profiles of ADT angles attain zero (0) value at the end of the contour, but acquire non-zero magnitude in the intermediate ϕ values.

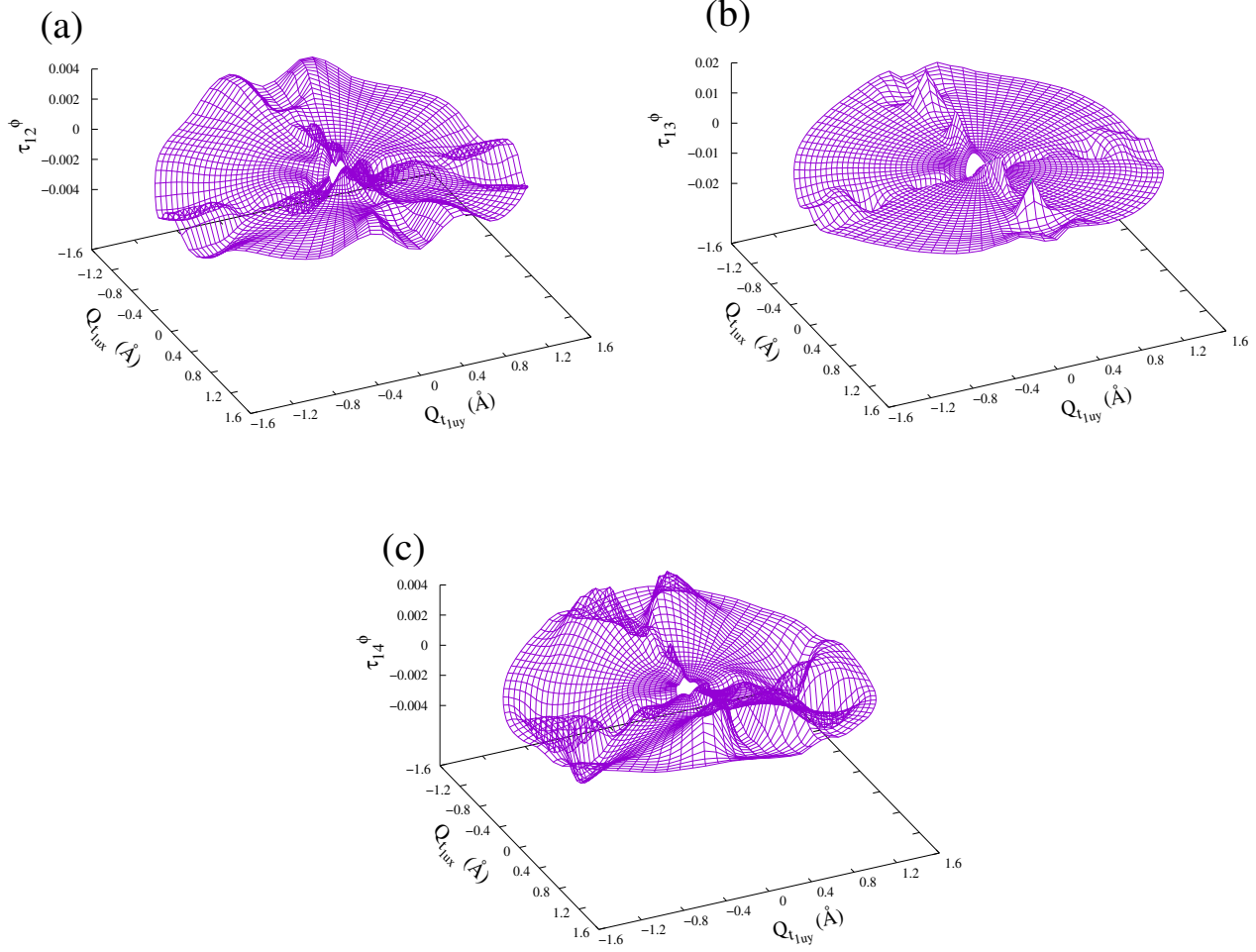


Fig. 9: 2D variation of ϕ component of NACTs, namely, (a) τ_{12}^ϕ , (b) τ_{13}^ϕ and (c) τ_{14}^ϕ are presented over $Q_{t1ux} - Q_{t1uy}$ plane. For all cases, the NACT profiles do not exhibit any singularity over the chosen domain of nuclear CS.

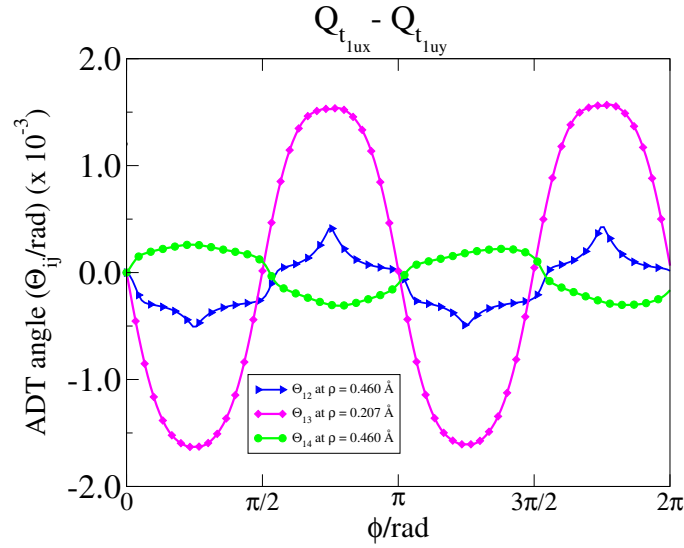
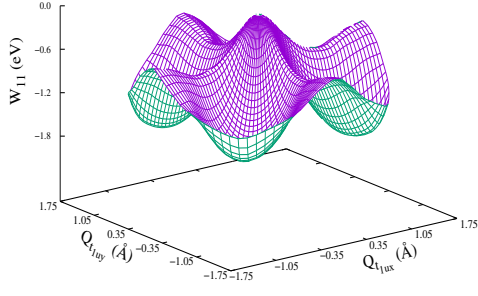


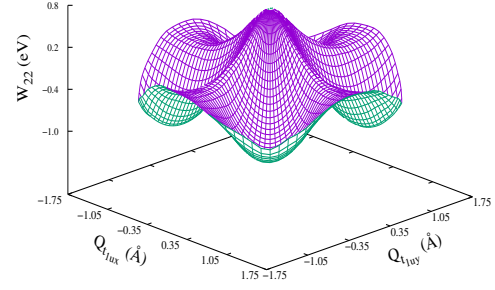
Fig. 10: 1D variation of ADT angles, namely, Θ_{12} , Θ_{13} and Θ_{14} for $Q_{t1ux} - Q_{t1uy}$ pairs are presented along the angular coordinate, ϕ for fixed values of ρ acquiring the magnitude of zero (0) at the end of the contour.

For $Q_{t1ux} - Q_{t1uy}$ pair of normal modes, path II (see Section S9 of the ESI) is employed to compute the diabatic Hamiltonian over 2D nuclear planes. While carrying out such calculation, the computed ADT matrices are employed in the similarity transformation (see Eq. 9) to obtain the diabatic PESs matrices. Some representative diabatic PESs (W_{11} and W_{22}) and coupling (W_{12}) are depicted in Figure 11 over the nuclear plane, $Q_{t1ux} - Q_{t1uy}$.

(a)



(b)



(c)

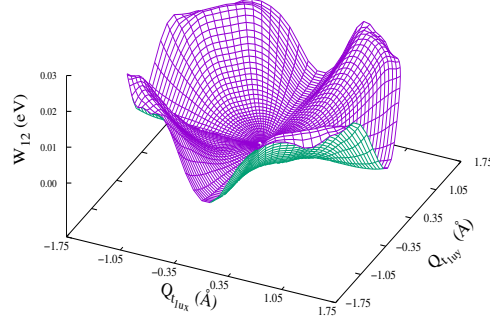


Fig. 11: For $Q_{t1ux} - Q_{t1uy}$ plane of TiO_6^{8-} unit of BaTiO_3 crystal, 2D functional forms of diabatic surfaces, namely, (a) W_{11} and (b) W_{22} , and the associated diabatic coupling, (c) W_{12} are presented, where all the quantities appear as well-behaved functions of nuclear coordinates.

5 Observables: Theoretical and Experimental Results

The literature on experimental evidence of electronic transition leading to satellite peak in dielectric function is absent, which may be due to the negligibly small JT stabilisation energy (0.0182 eV) arising from the JT-splitted triply degenerate electronic state T_{1u} . The experimental prediction of ferroelectricity of BaTiO₃ has been explored using the pseudo Jahn-Teller effect on ground electronic states through $A_{1g} - T_{1u}$ interaction, that has been studied in present and other theoretical calculation also. We employed *ab initio* calculated adiabatic PES and BBO based diabatic Hamiltonian to depict the nature of spontaneous polarisation and photoemission spectra, respectively.

5.1 Photoemission Spectra

We intend to probe the Jahn-Teller (JT) and pseudo Jahn-Teller (PJT) effect arising from electron-nuclear couplings in photoemission (PE) spectra, specifically engaging the diabatic PESs of transition metal oxide TiO₆⁸⁻ constructed with octahedral as well as all possible distorted geometries. In this investigation, we explore how the ground (A_{1g}) and excited (T_{1u}) electronic states of TiO₆⁸⁻ are influenced due to the interaction through the nuclear motion of the t_{1u} and t_{2g} normal modes or vice versa, where six two-dimensional (2D) nuclear planes, namely $Q_{t_{1ux}} - Q_{t_{1uy}}$, $Q_{t_{1uy}} - Q_{t_{1uz}}$, $Q_{t_{1uz}} - Q_{t_{1ux}}$, $Q_{t_{2gx}} - Q_{t_{2gy}}$, $Q_{t_{2gy}} - Q_{t_{2gz}}$ and $Q_{t_{2gz}} - Q_{t_{2gx}}$ are considered in the diabatic Hamiltonian. Since the electron-nuclear couplings are explicitly incorporated into the diabatic PESs matrices of TiO₆⁸⁻, those PESs matrices are used to carry out the TDDVR quantum dynamical calculations for elucidation of the PE spectra. The TDDVR basis set (grid points) for t_{1u} and t_{2g} normal modes are optimized using a wide range of basis functions starting from (3,3,3,3,3,3) [729 grid points] to (15,15,15,15,15,15) [1,13,90,625 grid points], where the set (13,7,7,13,11,11) [10,02,001 grid points] leads to converged PE spectral profile. In Section S11 of the ESI, a detailed discussion on the convergence analysis with suitable diagram is depicted in Figure S8. The quantum dynamical calculations are initiated by the wavepacket $[\Xi(0)]$, modelled as a product of Gaussian wavepackets (GWPs) representing the normal modes (t_{1u} and t_{2g}) of the TiO₆⁹⁻ anion. Such product type wavepacket is placed either on the electronic state A_{1g} or on the T_{1u} state(s) of TiO₆⁸⁻ and for each case, four state dynamical calculation has been performed. The time - dependent wavefunction is employed to calculate the corresponding autocorrelation functions at different time (see Eq. 18b), which on Fourier transformation (see Eq. 19) generates distinct spectral profiles for each state. Furthermore,

the convolution of these individual state spectra yields the comprehensive spectral envelope of the TiO_6^{8-} complex. Though the comparison is made between the calculated PE spectra for the A_{1g} and T_{1u} states of TiO_6^{8-} unit and the experimentally observed photoemission¹⁶ peaks for the BaTiO_3 complex, this is an approximation, but the other theoretical⁹² spectra for TiO_6^{8-} unit is appropriate. Since the ionization effect is naturally included in the experimental profile, this comparison with theoretical one is only within approximation. Figure 12 demonstrates the peak positions of the photoemission spectra of an isolated TiO_6^{8-} anion in comparison with experimental¹⁶ spectra of BaTiO_3 lattice and other theoretical⁹² spectra of TiO_6^{8-} unit, where the present diabatic surface matrix is derived from MRCI(SD)-based APESs as well as CASSCF-based DDR calculated NACTs for TiO_6^{8-} unit. The vertical dotted lines also depict the agreement of the peaks at 1.05 and 3.80 eV. Also note that the difference between the two peak positions in the spectrum (~ 2.75 eV) closely matches with the calculated global stabilization energy of 2.582 eV, which is attributed to the PJT interactions. At this point, it is important to note that since the TiO_6^{8-} is a unit cell of an infinite crystal, BaTiO_3 , the “actual” spectra will be broadened enough due to the dissipation of energy through neighbouring units. Thereby, it is necessary to introduce appropriate value of τ in the autocorrelation functions (see Eqs. 20 and 21) so that the damping of energy is quite fast and efficient leading to the PE spectra. This study yields valuable insights for the analysis and interpretation of the observed phenomena, contributing to the wider understanding of the intricate electronic and vibrational interactions in transition metal oxides, but brings little understanding on the nature of cooperative effect originating from the crystal.

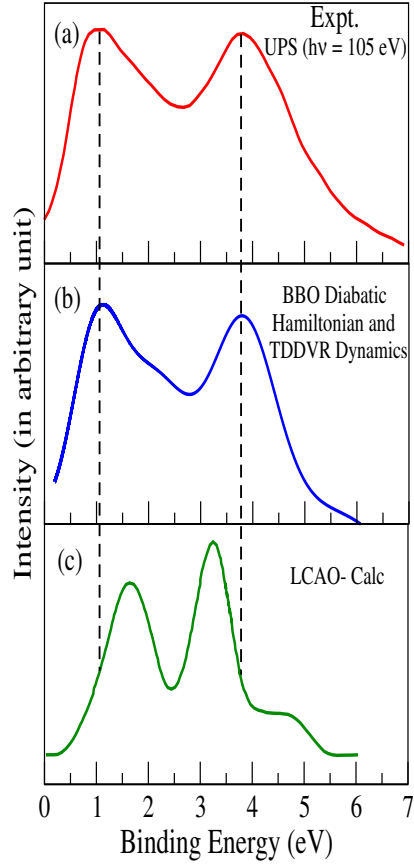


Fig. 12: Comparison between experimental valence electronic spectra and theoretical spectra: (a) UPS spectra of BaTiO_3 single crystal measured by Cord and coworkers¹⁶, (b) present work and (c) calculation of bulk BaTiO_3 by Pertosa *et al.*⁹²

5.2 Ferroelectricity

In ferroelectric materials, the spontaneous change of polarization occurs due to the displacement of positive and negative charges within each TiO_6^{8-} unit of the crystal lattice when the material undergoes a phase transition below its critical temperature known as the Curie temperature (T_C).⁹³ Below T_C , due to the structural change of unit cell, the crystal structure becomes non-centrosymmetric allowing the formation of permanent electric dipole(s). As the temperature increases approaching to T_C , the structural distortion diminishes and undergoes transition from a tetragonal to fully cubic phase, where such transition is accompanied by a second order phase change.

The numerical solution of Eq. 23 employing newly calculated adiabatic PES (see Section 4.2) provides insights into the system's behaviour on ferroelectricity as shown in Figure 13. We find that the theoretical calculated Curie temperature ($T_C \simeq 350$ K) of TiO_6^{8-} unit of barium titanate in Figure 13 closely matches with other theoretical^{94,95} and experimentally⁹⁶ results for the same crystal (see Figures S9, S10 and S11 in Section S12 of the ESI).

It appears that the PJT effect is the origin of polar instability within a single unit TiO_6^{8-} of the perovskite crystal. This instability leads to an off-centre displacement of the transition metal ion (Ti^{4+}), accompanied by significant polarization of valence-shell electronic states and a counter-phase displacement of neighbouring oxygen atoms. The polar distortion is triggered by vibronic PJT coupling between the ground and the excited electronic states of opposite parity, strengthening the covalent bonds between the transition metal and nearby oxygen atoms.

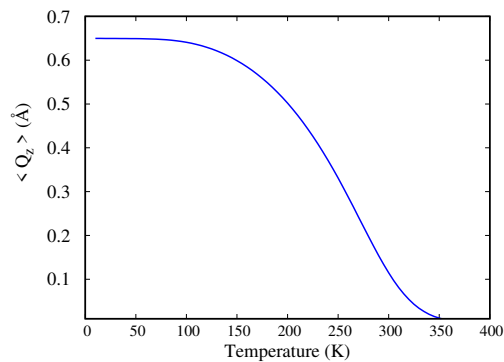


Fig. 13: The order Parameter, $\langle Q_z \rangle$ in the tetragonal phase exhibit gradual decline, culminating in the vanishing off-centre displacement of titanium ion (Ti^{4+}) at $T = 350$ K, indicative of second-order phase transition.

6 Conclusion

We utilize the coupled cluster method (CCSD/ANO-R1) as implemented in the MOLPRO quantum chemistry package to compute the frequencies of the triply degenerate t_{2g} and t_{1u} vibrational modes of an octahedral TiO_6^{8-} unit of a BaTiO_3 crystal. With these frequencies and displacement vectors of the normal modes for the TiO_6^{8-} unit of BaTiO_3 crystal, *ab initio* based adiabatic PESs (MRCI(SD)) and NACTS (DDR) are calculated to explore: (a) how the triply degenerate t_{2g} vibrational modes lead to JT distortion of the T_{1u} symmetric excited electronic states and (b) at what extent PJT interactions are observed between A_{1g} and T_{1u} states along t_{1u} vibrational modes. In our calculation, it appears that the lowest sheet of T_{1u} state is stabilized only by 0.0182 eV due to JT distortion, whereas the PJT interactions among A_{1g} and T_{1u} states stabilize the A_{1g} state of the order ~ 2.582 eV at $Q_{t_{1ux}} = Q_{t_{1uy}} = Q_{t_{1uz}} = \pm 0.51 \text{ \AA}$ with eight such global minima over the nuclear CS.

The couplings (NACTs) among the electronic states (A_{1g} and T_{1u}) along the normal modes (t_{2g} and t_{1u}) are evaluated by CASSCF based DDR methodology. While solving the ADT equation (Eqs. 10 and 11) using *ab initio* calculated NACTs, it is observed that the mixing angles (Θ_{23} or Θ_{34}) reach π (see Figure 4) at the completion of a closed contour ($\phi = 2\pi$), indicating the presence of enclosed JT CI. Conversely, the mixing angles (Θ_{12} or Θ_{13} or Θ_{14}) attain zero (see Figure 10) at the end of a closed contour ($\phi = 2\pi$), indicative of encapsulated PJT interactions. Furthermore, the presence of such CIs is confirmed by the sign inversion of the diagonal elements of the ADT matrices [A_{11} ($=A_{22}$)]. Finally, these ADT matrices facilitate the generation of smooth, single-valued, and continuous diabatic PESs and couplings.

We construct diabatic PESs and couplings over six (6) pairs of normal modes and carried out TD-DVR dynamics with optimized time-dependent basis sets to generate photoemission (PE) spectral profiles for combined four electronic states (A_{1g} and T_{1u}). The calculated spectra show reasonably good agreement with experimental profile¹⁶, even though the former one is obtained from single TiO_6^{8-} unit of BaTiO_3 crystal lattice and the later is measured for a single crystal of BaTiO_3 . Though the PJT effect introduces polar instability within a single unit TiO_6^{8-} , the cooperative effect of the crystal could be due to higher order polarisation arising from the environment of the lattice. Finally, we also calculate spontaneous polarization leading to ferroelectric properties in BaTiO_3 below the Curie temperature using adiabatic PESs, revealing the pseudo Jahn-Teller effect as the origin of polar instability and off-centre displacement of transition metal ions. Our inves-

tigation underscores the effectiveness of first principles-based BBO theory coupled with TDDVR methodology in elucidating the effect of nonadiabaticity on spectral profiles and the use of mean-field Hamiltonian (see Eqs. 22 and 23) for ferroelectric properties of TiO_6^{8-} unit of BaTiO_3 crystal lattice.

Electronic Supplementary Information

- A detailed theoretical description of TiO_6^{8-} within BaTiO_3 is presented in the Electronic Supplementary Information (ESI). This includes figures showing Adiabatic Potential Energy Curves (PECs) and Non-Adiabatic Coupling Terms (NACTs) as well as path integrals and the convergence of photoemission (PE) spectra. Moreover, both experimental and theoretical curves depicting spontaneous polarization variation with temperature are provided. Additionally, an overview of the Time-Dependent Discrete Variable Representation (TDDVR) Formalism is included in the ESI.

Acknowledgements

M.K.S acknowledges NBCFDC, Govt. of India, Ministry of Social Justice and Empowerment for research fellowship. S.M thanks IACS for research funding and MANIT, Bhopal for the seed grant. S.R is thankful to SERB through project no. SRG/2023/001624. S.A thanks SERB through project no. CRG/2023/000611 and IACS for the research funding and IACS for CRAY supercomputing facility.

Electronic Supplementary Information

S1 Conditions for the JT and PJT Interactions

While exploring the conditions to understand the properties related to the distortions of TiO_6^{8-} unit of BaTiO_3 crystal, it appears that the vibrational modes (t_{2g} and t_{1u}) are responsible for Jahn-Teller (JT) and pseudo Jahn-Teller (PJT) interactions. On the other hand, the Ti^{4+} ion of TiO_6^{8-} unit having a d^0 electronic configuration leads to a non-degenerate ground state (A_{1g}), whereas the first excited state is triply degenerate (T_{1u}). The JT and PJT effects originate due to the coupling of electronic state with vibrational modes of appropriate symmetry. In other words, the direct product of irreducible representations for the electronic state and the vibrational mode contains the totally symmetric representation (A_{1g}). The JT distortion takes place between ${}^1T_{1u}$ states via t_{2g} normal modes:

$$A_{1g} \in t_{2g} \otimes [(T_{1u})^2] \equiv g \otimes u \otimes u,$$

whereas the PJT effect involves the coupling between the non-degenerate ground state (A_{1g}) and an excited state (T_{1u}) via vibrational modes (t_{1u}):

$$A_{1g} \in t_{1u} \otimes [A_{1g} \otimes T_{1u}] \equiv u \otimes g \otimes u.$$

Though our calculations reveal that the JT distortion due to interaction of t_{2g} normal modes with T_{1u} electronic states is negligibly small, the PJT stabilization for the coupling of t_{1u} modes with A_{1g} and ${}^1T_{1u}$ electronic states is significant. Moreover, *ab initio* calculation along other u -symmetric normal modes (t_{2u} and other set of t_{1u}) yield approximately the same stabilization energy (-0.65 eV) and thereby, one representative set of u -symmetric normal modes is chosen for the present calculation. This selection simplifies the calculation as predicted before⁵ to depict the effect of PJT stabilization on photoemission spectra and ferroelectric properties.

S2 Adiabatic to Diabatic Transformation Equation: Curl Condition

In adiabatic Representation, the kinetically coupled SE can be written as:

$$-\frac{\hbar^2}{2} \left(\vec{\nabla}_R + \vec{\tau} \right)^2 \psi^{ad} + (U - E) \psi^{ad} = 0. \quad (\text{S1})$$

Using the following transformation:

$$\psi^{ad} = A\psi^d, \quad (\text{S2})$$

with ψ^{ad} and ψ^d as adiabatic and diabatic nuclear wavefunctions, respectively and ‘ A ’ being the adiabatic-to-diabatic transformation matrix, Eq. S1 turns into:

$$-\frac{\hbar^2}{2} \left(\vec{\nabla}_R + \vec{\tau} \right)^2 A\psi^d + (U - E)A\psi^d = 0, \quad (\text{S3})$$

which appears as:

$$\begin{aligned} -\frac{\hbar^2}{2} \left[A \nabla_R^2 \psi^d + 2(\vec{\nabla}_R A + \vec{\tau} A) \cdot \vec{\nabla}_R \psi^d + \left\{ (\vec{\tau} + \vec{\nabla}_R) \cdot (\vec{\nabla}_R A + \vec{\tau} A) \right\} \psi^d \right] A\psi^d \\ + (U - E)A\psi^d = 0. \end{aligned} \quad (\text{S4})$$

If the following constrain is imposed,

$$\vec{\nabla}_R A + \vec{\tau} A = 0, \quad (\text{S5})$$

Eq. S4 reduces to the form as given below:

$$-\frac{\hbar^2}{2} A \nabla_R^2 \psi^d + (U - E)A\psi^d = 0. \quad (\text{S6})$$

On the other hand, when Eq. S5 is left multiplied by A^\dagger and the daggered (\dagger) of Eq. S5 is right multiplied by A , we obtain:

$$A^\dagger \vec{\nabla}_R A + A^\dagger \vec{\tau} A = 0, \quad (\text{S7a})$$

$$(\vec{\nabla}_R A^\dagger) A - A^\dagger \vec{\tau} A = 0, \quad (\text{S7b})$$

and then, on adding Eqs. S7a and S7b, we obtain:

$$\begin{aligned}
A^\dagger \vec{\nabla}_R A + (\vec{\nabla}_R A^\dagger) A &= 0, \\
\Rightarrow \vec{\nabla}_R (A^\dagger A) &= 0, \\
\Rightarrow A^\dagger A &= \text{const},
\end{aligned} \tag{S8}$$

which defines A is an orthogonal matrix.

Therefore, we left multiply Eq. S6 by A^\dagger and obtain the diabatic representation of SE:

$$-\frac{\hbar^2}{2} \nabla_R^2 \psi^d + (W - E) \psi^d = 0, \tag{S9}$$

where

$$W = A^\dagger U A. \tag{S10}$$

The couplings between electronic states are incorporated within the potential energy matrix (W)⁹⁷.

While performing BBO-based diabaticization of adiabatic PESs and NACTs, it is essential to verify whether the number of electronic states (N) within the relevant domain of nuclear space can be considered a “true” SHS for required numerical accuracy. The existence of such SHS can be assessed by evaluating the matrix elements of Curl Condition²⁰ associated with the NACTs as outlined below. For any pair of nuclear coordinates (p and q), the scalar form of Eq. S5 can be expressed as:

$$\nabla_p A + \tau_p A = 0, \tag{S11}$$

$$\nabla_q A + \tau_q A = 0, \tag{S12}$$

and by taking cross-derivatives to Eqs. S11 and S12, we obtain:

$$\nabla_q \nabla_p A + \left(\frac{\partial}{\partial q} \tau_p \right) A + \tau_p \frac{\partial}{\partial q} A = 0, \tag{S13a}$$

$$\nabla_p \nabla_q A + \left(\frac{\partial}{\partial p} \tau_q \right) A + \tau_q \frac{\partial}{\partial p} A = 0. \tag{S13b}$$

Since the matrix element of A are analytic functions of the nuclear coordinates (p and q) and $\nabla_q \nabla_p A = \nabla_p \nabla_q A$, we obtain the following Curl Condition:

$$\frac{\partial}{\partial p} \tau_q^{ij} - \frac{\partial}{\partial q} \tau_p^{ij} = (\tau_q \tau_p)_{ij} - (\tau_p \tau_q)_{ij}, \quad (\text{S14})$$

where the matrix elements (analogous to Yang-Mills field) over $p - q$ plane are represented as:

$$F_{pq}^{ij} = \left[\frac{\partial}{\partial p} \tau_q^{ij} - \frac{\partial}{\partial q} \tau_p^{ij} \right] - \left[(\tau_q \tau_p)_{ij} - (\tau_p \tau_q)_{ij} \right] = Z_{pq}^{ij} - C_{pq}^{ij}. \quad (\text{S15})$$

When the sub-space is complete, the magnitude of F_{pq}^{ij} should be zero (0) over the relevant domain of nuclear configuration space, ensuring that the non-removable component of the NACTs becomes negligibly small. If this condition is not satisfy for the chosen SHS, it becomes necessary to enlarge the sub-space in order to diabatize the SE in a “true” sense, achieving the desired level of accuracy.

S3 Explicit Expression of ADT Equations and NACTs for Four state ($N = 4$) sub-Hilbert space²⁹

S3.1 ADT Equations

$$\begin{aligned} \nabla_R \Theta^{12} &= -\tau^{12} - \sin \Theta^{12} \tan \Theta^{13} \tau^{13} - \cos \Theta^{12} \tan \Theta^{13} \tau^{23} - \sin \Theta^{12} \sec \Theta^{13} \tan \Theta^{14} \tau^{14} - \cos \Theta^{12} \sec \Theta^{13} \tan \Theta^{14} \tau^{24} \\ \nabla_R \Theta^{13} &= -\cos \Theta^{12} \tau^{13} + \sin \Theta^{12} \tau^{23} - \cos \Theta^{12} \sin \Theta^{13} \tan \Theta^{14} \tau^{14} + \sin \Theta^{12} \sin \Theta^{13} \tan \Theta^{14} \tau^{24} - \cos \Theta^{13} \tan \Theta^{14} \tau^{34} \\ \nabla_R \Theta^{23} &= -\cos \Theta^{13} [\tau^{13} \sin \Theta^{12} \sec^2 \Theta^{13} + \cos \Theta^{23} \sec \Theta^{14} (\tau^{34} - \tau^{24} \sin \Theta^{12} \tan \Theta^{13}) \tan \Theta^{24} \\ &\quad + \sin \Theta^{12} \sec \Theta^{13} \tan \Theta^{13} \tau^{14} \tan \Theta^{14} + \sin \Theta^{23} \tau^{14} \sec \Theta^{14} \tan \Theta^{24} + \cos \Theta^{12} \{ \tau^{23} \sec^2 \Theta^{13} \\ &\quad + \tan \Theta^{13} \cos \Theta^{23} \tau^{14} \sec \Theta^{14} \tan \Theta^{24} + \sec \Theta^{13} (\tan \Theta^{13} \tau^{24} \tan \Theta^{14} \\ &\quad + \sin \Theta^{23} \tau^{24} \sec \Theta^{14} \tan \Theta^{24}) \}] \\ \nabla_R \Theta^{14} &= -\cos \Theta^{12} \cos \Theta^{13} \tau^{14} + \sin \Theta^{12} \cos \Theta^{13} \tau^{24} + \sin \Theta^{13} \tau^{34} \\ \nabla_R \Theta^{24} &= \sin \Theta^{23} (-\sin \Theta^{12} \sin \Theta^{13} \tau^{24} \sec \Theta^{14} + \cos \Theta^{13} \tau^{34} \sec \Theta^{14}) - \sin \Theta^{12} \cos \Theta^{23} \tau^{14} \sec \Theta^{14} \\ &\quad + \cos \Theta^{12} (\sin \Theta^{13} \sin \Theta^{23} \tau^{14} \sec \Theta^{14} - \cos \Theta^{23} \tau^{24} \sec \Theta^{14}) \\ \nabla_R \Theta^{34} &= \sin \Theta^{12} \{ -\sin \Theta^{23} \tau^{14} \sec \Theta^{14} \sec \Theta^{24} + \sin \Theta^{13} \cos \Theta^{23} \tau^{24} \sec \Theta^{14} \sec \Theta^{24} \} + \cos \Theta^{12} [-\sec \Theta^{24} \\ &\quad \{ \sin \Theta^{13} \cos \Theta^{23} \tau^{14} \sec \Theta^{14} + \sin \Theta^{23} \tau^{24} \sec \Theta^{14} \}] - \cos \Theta^{13} \cos \Theta^{23} \tau^{34} \sec \Theta^{14} \sec \Theta^{24} \end{aligned}$$

S3.2 NACTs

$$\begin{aligned}
\tau^{12} &= -\cos \Theta^{13} \cos \Theta^{23} \cos \Theta^{14} \cos \Theta^{24} \nabla_R \Theta^{12} - \sin \Theta^{23} \cos \Theta^{14} \cos \Theta^{24} \nabla_R \Theta^{13} - \sin \Theta^{24} \nabla_R \Theta^{14} \\
\tau^{13} &= \cos \Theta^{13} \sin \Theta^{23} \cos \Theta^{14} \cos \Theta^{34} \nabla_R \Theta^{12} + \cos \Theta^{13} \cos \Theta^{23} \cos \Theta^{14} \sin \Theta^{24} \sin \Theta^{34} \nabla_R \Theta^{12} - \cos \Theta^{23} \cos \Theta^{14} \cos \Theta^{34} \nabla_R \Theta^{13} \\
&\quad + \sin \Theta^{23} \cos \Theta^{14} \sin \Theta^{24} \sin \Theta^{34} \nabla_R \Theta^{13} \\
\tau^{23} &= -\sin \Theta^{13} \cos \Theta^{24} \cos \Theta^{34} \nabla_R \Theta^{12} - \cos \Theta^{13} \sin \Theta^{23} \sin \Theta^{14} \sin \Theta^{24} \cos \Theta^{34} \nabla_R \Theta^{12} - \cos \Theta^{13} \cos \Theta^{23} \sin \Theta^{14} \sin \Theta^{34} \nabla_R \Theta^{12} \\
&\quad + \cos \Theta^{23} \sin \Theta^{14} \sin \Theta^{24} \cos \Theta^{34} \nabla_R \Theta^{13} - \sin \Theta^{23} \sin \Theta^{14} \sin \Theta^{34} \nabla_R \Theta^{13} - \cos \Theta^{24} \cos \Theta^{34} \nabla_R \Theta^{23} - \sin \Theta^{34} \nabla_R \Theta^{24} \\
\tau^{14} &= -\cos \Theta^{13} \sin \Theta^{23} \cos \Theta^{14} \sin \Theta^{34} \nabla_R \Theta^{12} + \cos \Theta^{13} \cos \Theta^{23} \cos \Theta^{14} \sin \Theta^{24} \cos \Theta^{34} \nabla_R \Theta^{12} + \cos \Theta^{23} \cos \Theta^{14} \sin \Theta^{34} \nabla_R \Theta^{13} \\
&\quad + \sin \Theta^{23} \cos \Theta^{14} \sin \Theta^{24} \cos \Theta^{34} \nabla_R \Theta^{13} - \cos \Theta^{24} \cos \Theta^{34} \nabla_R \Theta^{14} \\
\tau^{24} &= \sin \Theta^{13} \cos \Theta^{24} \sin \Theta^{34} \nabla_R \Theta^{12} + \cos \Theta^{13} \sin \Theta^{23} \sin \Theta^{14} \sin \Theta^{24} \sin \Theta^{34} \nabla_R \Theta^{12} - \cos \Theta^{13} \cos \Theta^{23} \sin \Theta^{14} \cos \Theta^{34} \nabla_R \Theta^{12} \\
&\quad - \cos \Theta^{23} \sin \Theta^{14} \sin \Theta^{24} \sin \Theta^{34} \nabla_R \Theta^{13} - \sin \Theta^{23} \sin \Theta^{14} \cos \Theta^{34} \nabla_R \Theta^{13} + \cos \Theta^{24} \sin \Theta^{34} \nabla_R \Theta^{23} - \cos \Theta^{34} \nabla_R \Theta^{24} \\
\tau^{34} &= -\sin \Theta^{13} \sin \Theta^{24} \nabla_R \Theta^{12} + \cos \Theta^{13} \sin \Theta^{23} \sin \Theta^{14} \cos \Theta^{24} \nabla_R \Theta^{12} - \cos \Theta^{23} \sin \Theta^{14} \cos \Theta^{24} \nabla_R \Theta^{13} \\
&\quad - \sin \Theta^{24} \nabla_R \Theta^{23} - \nabla_R \Theta^{34}
\end{aligned}$$

S4 Adiabatic Potential Energy Curves (PECs) and NACTs for TiO_6^{8-} unit of BaTiO_3 crystal

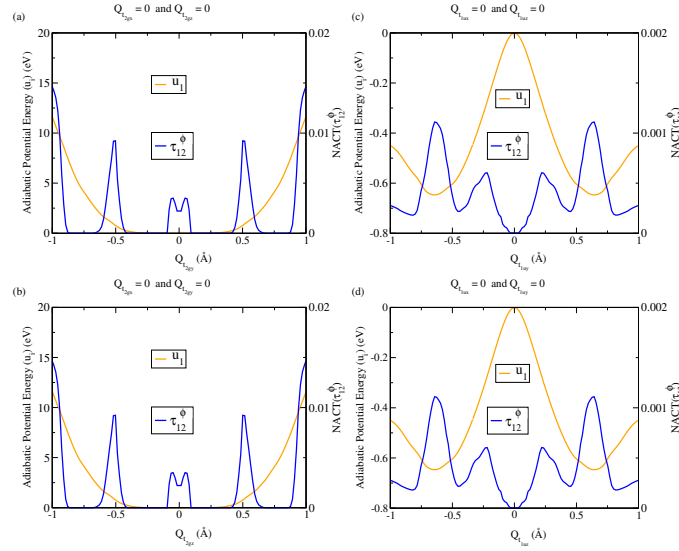


Fig. S1: For TiO_6^{8-} unit, 1D curves of lowest adiabatic PES (u_1) and the associated NACT (τ_{12}^ϕ) are presented along (a) Q_{t2gy} , (b) Q_{t2gz} , (c) Q_{t1uy} , and (d) Q_{t1uz} normal modes keeping the other normal modes fixed at zero (0).

S5 Local Topographic Parameters and Adiabatic Potential Energy Surfaces Around the 2-3 Conical Intersection (CI)

We have calculated the local topographic parameter at the geometry of one of the ‘2-3’ CI⁹⁸, where two independent geometrical distortions can linearly break the degeneracy, commonly known as *branching plane vectors*. These two vectors are mainly represented as \vec{g} (the half-difference between the gradients of the two intersecting states) and \vec{h} (the non-adiabatic coupling vectors between the two states). In order to calculate the local topographic parameters (tilt parameters (s_x and s_y), pitch of cone (d_{gh}) and asymmetry of cone (Δ_{gh})) for a double cone, we have employed COLUMBUS quantum chemistry package⁹⁹, where the calculated parameters are tabulated below:

s_x (eV/Å)	s_y (eV/Å)	Δ_{gh}	d_{gh} (eV/Å)
-0.046	-0.004	0.012	0.005

On the basis of above local topographic parameters, the model double cone adiabatic potential energy surfaces (PESs) have been calculated using the following functional form:

$$U_2 = s_x \cdot x + s_y \cdot y - d_{gh} \left[\frac{x^2 + y^2}{2} + \Delta_{gh} \frac{(x^2 - y^2)}{2} \right]^{1/2} \quad (\text{S18})$$

$$U_3 = s_x \cdot x + s_y \cdot y + d_{gh} \left[\frac{x^2 + y^2}{2} + \Delta_{gh} \frac{(x^2 - y^2)}{2} \right]^{1/2} \quad (\text{S19})$$

and the associated PESs are represented in the following figure:

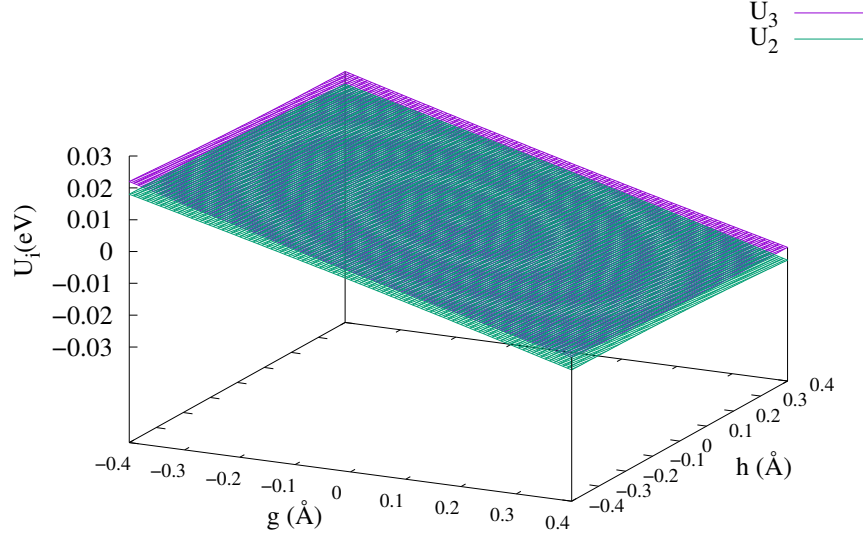


Fig. S2: Model adiabatic PESs around ‘2-3’ CI along two branching plane vectors (g and h)

Figure S2 shows that the calculated model PESs using topographic parameters vary linearly at the close vicinity of CI. In other words, degeneracy is lifted linearly around the ‘2-3’ CI indicating that the intersections are “conical” not glancing.

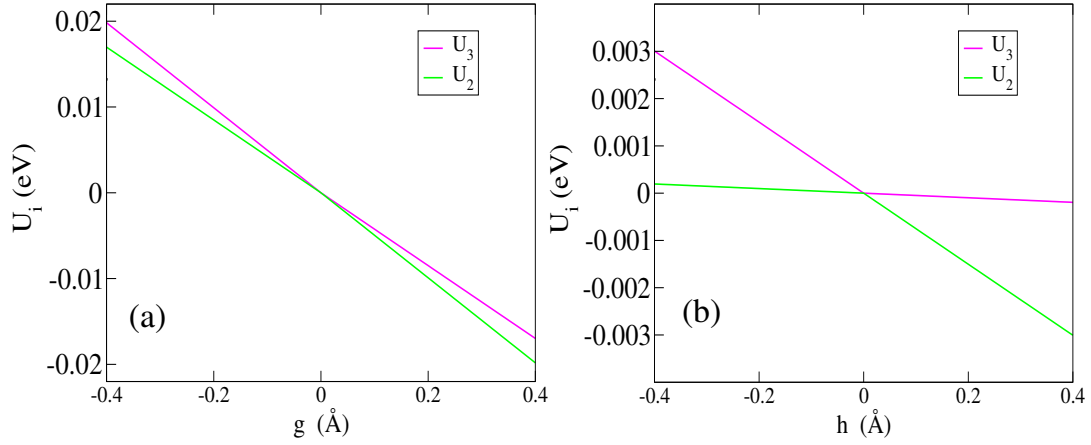


Fig. S3: 1D curves of model adiabatic PESs around ‘2-3’ CI are presented along branching plane vector (a) g and (b) h . In each case, the PECs are plotted while keeping the other coordinate fixed at zero: (a) $h = 0$ and (b) $g = 0$.

S6 The t_{1u} normal mode vibration of TiO_6^{-8} unit

The triply degenerate vibrational modes (t_{1u}) are purely bending modes along XZ , XY and YZ plane. In *ab-initio* calculation, two modes are chosen along X and Y direction to locate the PJT minima.

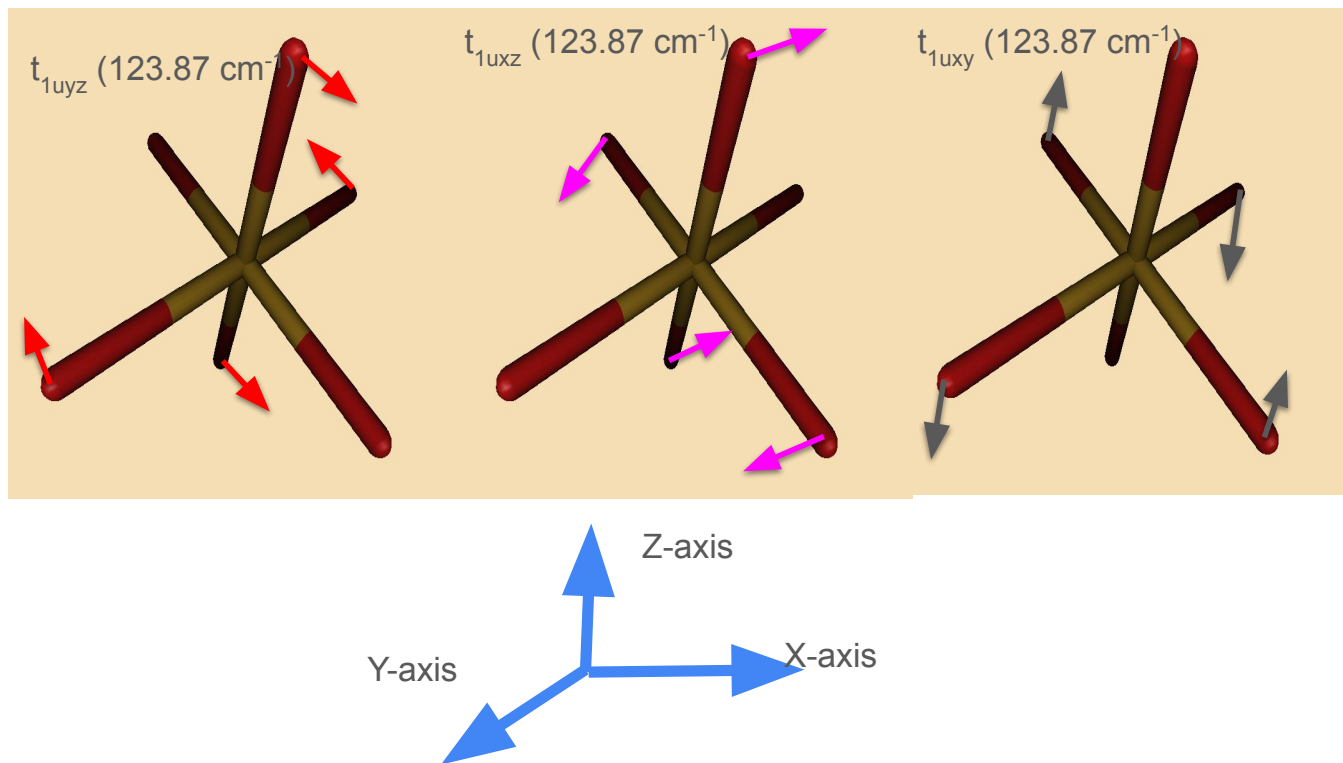


Fig. S4: Schematic picture of t_{1u} modes of TiO_6^{-8} calculated at CCSD level for O_h configuration ($\text{Ti-O} = 2.0 \text{ \AA}$). The calculated frequency is 123.87 cm^{-1} . The arrow shows the bending motion of Ti-O bond.

S7 Optimized Geometry of TiO_6^{-8} on the ground state

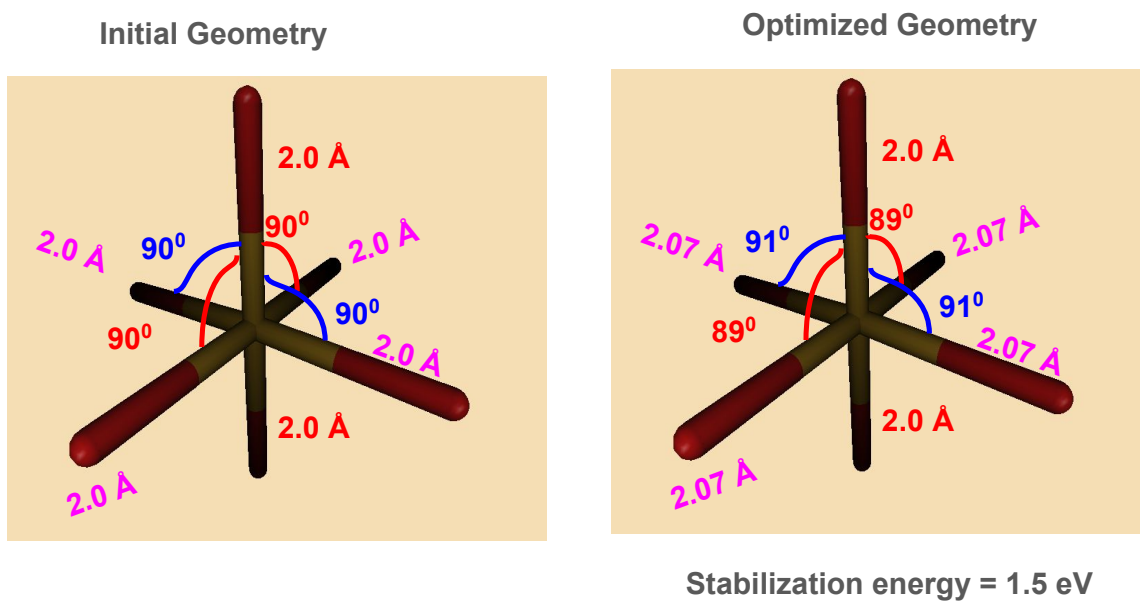


Fig. S5: The optimized geometry of TiO_6^{-8} on the ground state.

S8 Geometry of PJT Stabilized TiO_6^{-8} on the ground state

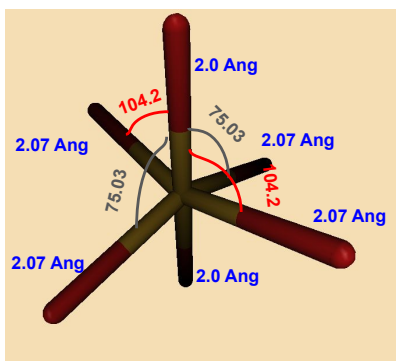


Fig. S6: The geometry of PJT stabilized TiO_6^{-8} on the ground state (extracted from *ab-initio calculation* at $\rho = 8.2$ and $\phi = 0$).

S9 Integration Paths for Stiff Differential Equations⁷¹

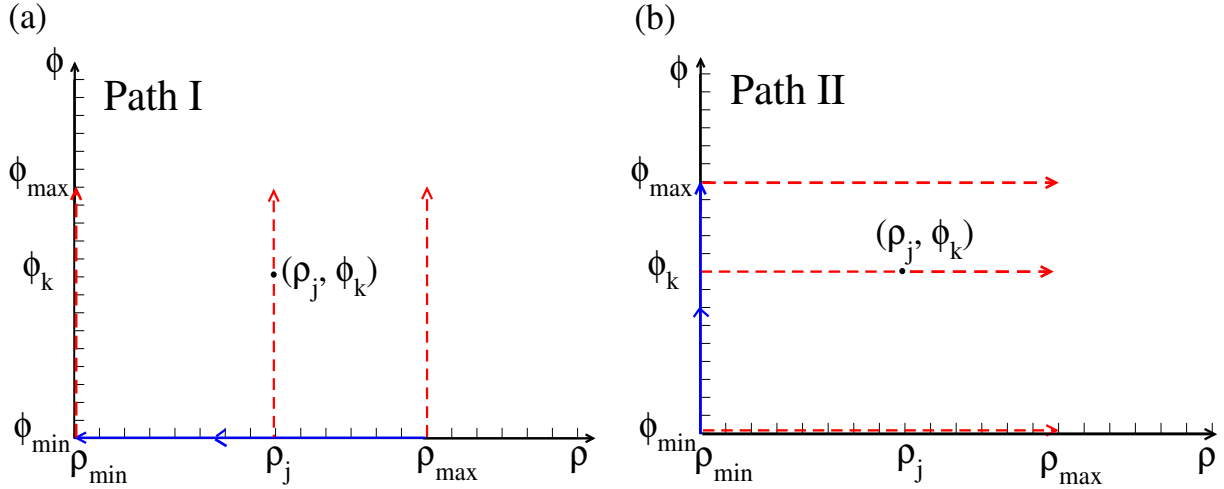


Fig. S7: Panels (a) and (b) depict the numerical solution of the stiff differential equations along path I and path II. The integration process involves solving the equations first along the bold (blue) line and subsequently along the dotted (red) lines in each case.

S10 An Overview on Time-Dependent Discrete Variable Representation (TDDVR) Formalism

The TDDVR formalism has been implemented over wide range of problems involving nuclear dynamics on low-dimensional model^{100,101} systems as well as multi-dimensional multi-surface chemical processes^{82,102–104}. While dealing with TDDVR dynamics in multi-dimensional multi-surface molecular systems, we can formulate the time-dependent Schrödinger Equation (TDSE) within the diabatic framework in the following manner,

$$i\hbar \frac{\partial}{\partial t} \Xi(\{Q_k\}, t) = [\hat{\mathbf{T}}_{nuc}\{Q_k\} + \hat{\mathbf{W}}(\{Q_k\})] \Xi(\{Q_k\}, t), \quad (\text{S20})$$

where $\hat{\mathbf{T}}_{nuc}\{Q_k\}$ ($= \hat{T}_{nuc}\{Q_k\} \cdot \mathbf{I}$) and $\hat{\mathbf{W}}(\{Q_k\})$ denote the kinetic energy operator and diabatic PES matrix, respectively, let say, expressed in terms of normal mode coordinates, $\{Q_k\}$. For systems

with N coupled electronic states, the nuclear wavefunction can be represented as follows,

$$\Xi(\{Q_k\}, t) \equiv \begin{pmatrix} \psi_1(\{Q_k\}, t) \\ \psi_2(\{Q_k\}, t) \\ \psi_3(\{Q_k\}, t) \\ \vdots \\ \psi_N(\{Q_k\}, t) \end{pmatrix} \quad (\text{S21})$$

where $\Xi(\{Q_k\}, t)$ is normalized $[\int \Xi^\dagger(\{Q_k\}, t) \Xi(\{Q_k\}, t) \prod_{k=1}^p dQ_k = 1]$ at any time t .

In TDDVR formalism, the wavefunction corresponding to the l^{th} PES, denoted as $\psi_l(\{Q_k\}, t)$ (see Eq. S21) is represented using TDDVR basis functions ($\chi_{i_k}(Q_k, t)$) for a total of p normal modes.

$$\psi_l(\{Q_k\}, t) = \sum_{i_1 i_2 \dots i_p} c_{i_1 i_2 \dots i_p, l}(t) \prod_{k=1}^p \chi_{i_k}(Q_k, t) \quad (\text{S22})$$

Alternatively, the TDDVR basis functions can be written in terms of Discrete Variable Representation (DVR) basis and time-evolving plane waves:

$$\chi_{i_k}(Q_k, t) = \phi(Q_k, t) \sum_{n=0}^{N_k} \zeta_n^*(x_{i_k}) \zeta_n(x_k) \quad (\text{S23})$$

$$= \sum_{n=0}^{N_k} \zeta_n^*(x_{i_k}) \Phi_n(Q_k, t), \quad (\text{S24})$$

where the plane wave takes the following form:

$$\phi(Q_k, t) = \pi^{1/4} \exp\left(\frac{i}{\hbar} \{p_{Q_k^c}(t)[Q_k - Q_k^c(t)]\}\right). \quad (\text{S25})$$

In the DVR basis functions, harmonic oscillator eigenfunctions are chosen as the primitive bases (Eq. S23),

$$\zeta_n(x_k) = \left(\frac{2ImA_k}{\pi\hbar}\right)^{1/4} \frac{1}{\sqrt{n!2^n\sqrt{\pi}}} \exp\{-(x_k)^2/2\} H_n(x_k), \quad (\text{S26})$$

where

$$x_k = \sqrt{\frac{2ImA_k}{\hbar}} (Q_k - Q_k^c(t)). \quad (\text{S27})$$

In a similar way, the roots of $N_{k^{th}}$ Hermite polynomial, $H_{N_k}(x_k)$ ¹⁰⁵ attain the following expression,

$$x_{i_k} = \sqrt{\frac{2ImA_k}{\hbar}} (Q_{i_k}(t) - Q_k^c(t)), \quad (\text{S28})$$

resulting into the following expression of TDDVR grid-points:

$$Q_{i_k}(t) = Q_k^c(t) + \sqrt{\frac{\hbar}{2ImA_k}} x_{i_k}. \quad (\text{S29})$$

It's important to note that while the centre of the wavepacket ($\{Q_k^c\}$) and its momentum ($\{p_{Q_k^c}\}$) are assumed to be time-varying, the imaginary part of the width (ImA_k) is introduced as time-independent.¹⁰⁶ In simpler terms, the time dependency arises from the TDDVR grid points, Q_{i_k} s, which are influenced by the variables, $Q_k^c(t)$ and $p_{Q_k^c}(t)$.

The Gauss-Hermite (G-H) basis functions for the k^{th} normal mode ($\Phi_n(Q_k, t)$ in Eq. S24) are confirmed to be orthonormal⁸³, with the ground state representing the Gaussian Wave Packet (GWP). Similarly, the TDDVR basis functions χ_{i_k} s in Eq. (S23) for the k^{th} mode adhere to orthogonality, although they do not constitute a normalized set⁸³.

By substituting the TDDVR representation of wavefunctions (Eqs. S21 - S28) in the TDSE (Eq. S20), we get the following form of TDDVR matrix equation for the l^{th} PES,

$$i\hbar \mathbf{A} \dot{\mathbf{C}}_1 = \mathbf{H}_{11}^t \mathbf{C}_1 + \mathbf{A} \sum_{l' \neq 1} \mathbf{W}_{1l'} \mathbf{C}_{l'} \quad (\text{S30})$$

which can be transformed into the following convenient (symmetric) form through a similarity transformation,

$$i\hbar \dot{\mathbf{D}}_1(t) = \mathbf{A}^{-1/2} \mathbf{H}_{11}^t \mathbf{A}^{-1/2} \mathbf{D}_1 + \sum_{l' \neq 1} \mathbf{W}_{1l'} \mathbf{D}_{l'} \quad (\text{S31})$$

where $\mathbf{D}_1 = \mathbf{A}^{1/2} \mathbf{C}_1$. The detailed expression of the TDDVR coefficients, $d_{i_1 i_2 \dots i_p, l}$ and the specific forms of various component matrices $\{\mathbf{X}^k\}$ and $\{\mathbf{Y}^k\}$ of \mathbf{H}^t are provided in our earlier articles^{68,69,83}. On the other hand, the center of the wavepacket ($\{Q_k^c\}$) and its momentum ($\{p_{Q_k^c}\}$) for the k^{th} mode involve the following classical equations of motion (EOMs):

$$\dot{Q}_k^c(t) = \frac{p_{Q_k^c}(t)}{\mu}, \quad (\text{S32})$$

$$\dot{p}_{Q_k^c}(t) = - \left. \frac{dW(\{Q_k\})}{dQ_k} \right|_{Q_k(t)=Q_k^c(t)}. \quad (\text{S33})$$

While deriving a first principle based explicit expression of $\dot{p}_{Q_k^c}$ for multi-dimensional multi-surface systems, it is necessary to employ the Dirac-Frenkel variational principle.^{68,69,83,107} Interested readers

may refer to the aforementioned works for a thorough explanation of the initialization of wavepackets and their subsequent propagation over the diabatic PESs.

S11 Convergence Test of TDDVR Basis Set for Spectral Profile

In this present work, while performing the dynamics and calculating the PE spectra of the titanate (TiO_6^{9-}) system, we have optimized the basis functions, starting with smaller one, such as (3,3,3,3,3,3) [729 grid points] and then, going to the larger sets, such as (15,15,15,15,15,15) [1,13,90,625 grid points], to find the best combination for accurate calculations in TDDVR dynamics. In the above sets, the sequence of grid points represents six modes (t_{2g} and t_{1u} normal modes) of fundamental vibrational frequencies. On the process of the convergence analysis to obtain the converged spectral profiles for combined four states (A_{1g} and T_{1u}) (13,7,7,13,11,11), total 10,02,001 number of grid points are involved. In order to explore such convergence, four representative PE spectra are shown in the Figure S8.

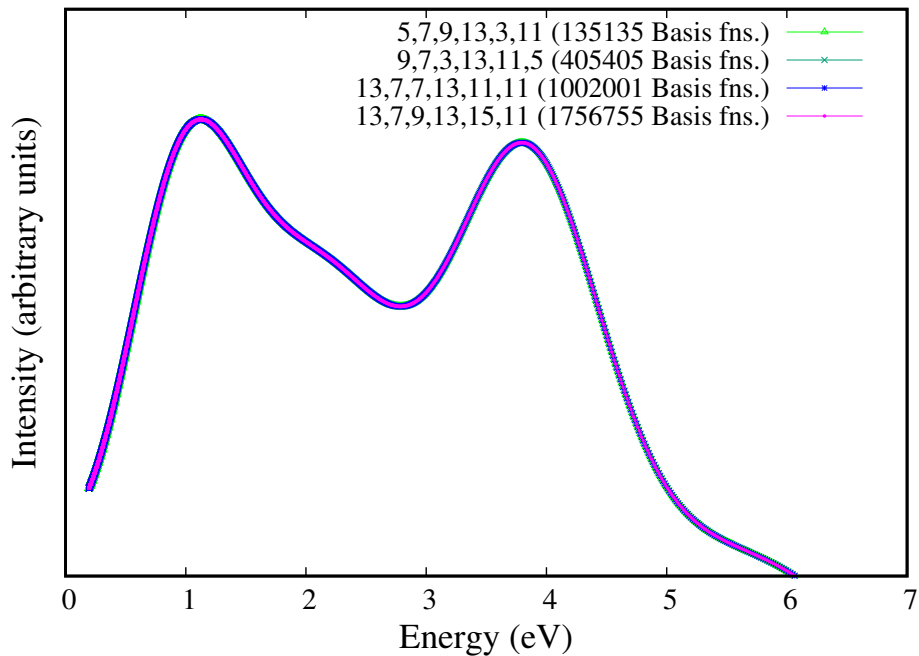


Fig. S8: TDDVR calculated spectra obtained from BBO based diabatic PESs are presented for four sets of basis functions. All sets are almost superimposed with each other and therefore, the set 13,7,7,13,11,11 is used as the optimized set of basis function.

S12 Theoretical and Experimental: Spontaneous Polarization vs Temperature

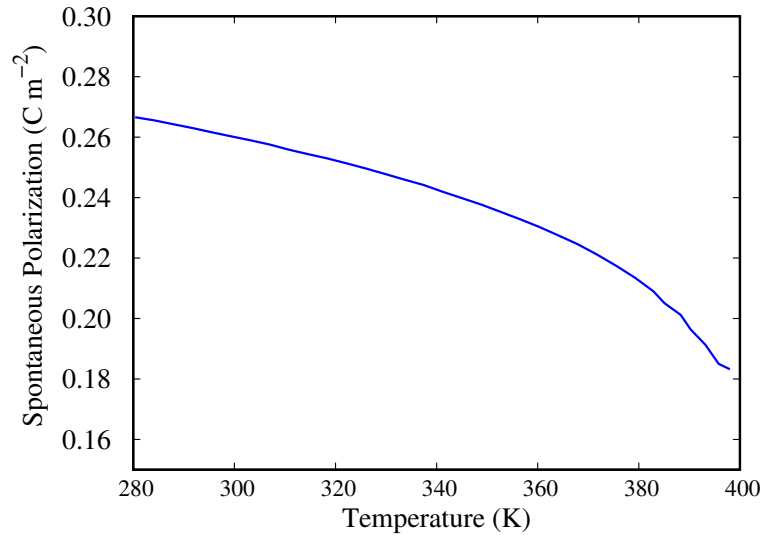


Fig. S9: Dependence of polarization on temperature for BaTiO₃ single crystal for tetragonal to cubic phase by Li *et al.*⁹⁴.

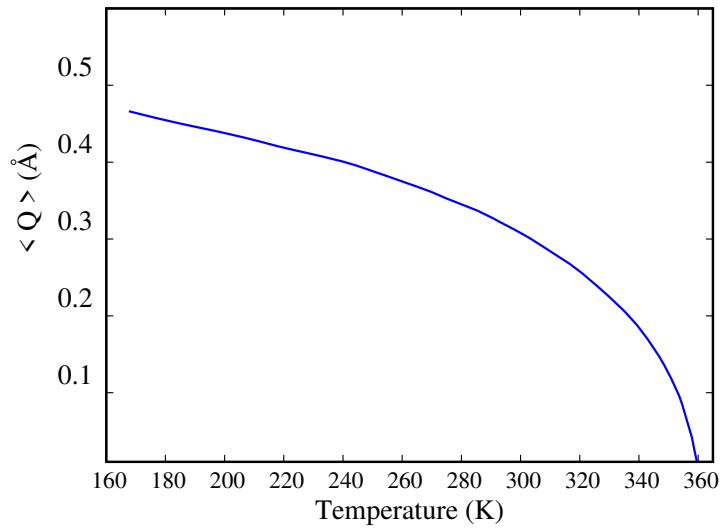


Fig. S10: Temperature dependence of the order parameter $\langle Q \rangle$ (in Å) from tetragonal to cubic phase by V. Polinger⁹⁵.

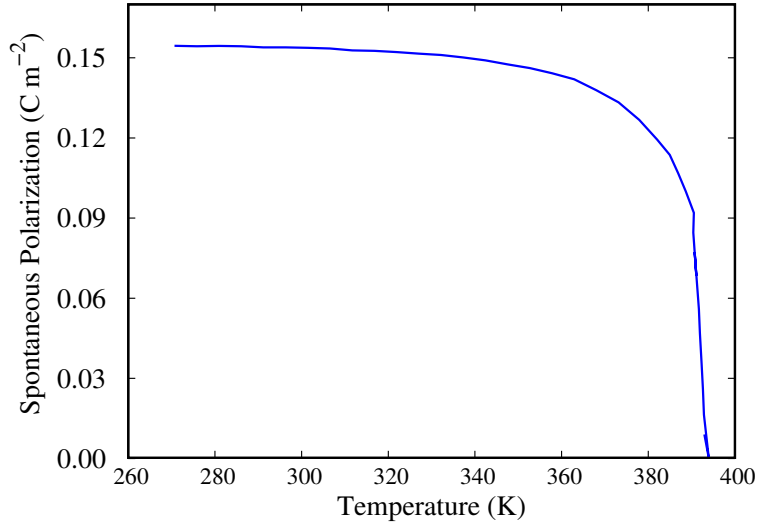


Fig. S11: Spontaneous polarization as a function of temperature for tetragonal to cubic phase by Walter J. Merz⁹⁶.

References

- [1] I. B. Bersuker, *Phys. Lett.*, 1966, **20**, 589–590.
- [2] A. Koleżyński and K. Tkacz-Śmiech, *Ferroelectrics*, 2005, **314**, 123–134.
- [3] Q.-J. Liu, N.-C. Zhang, F.-S. Liu, H.-Y. Wang and Z.-T. Liu, *Opt. Mater.*, 2013, **35**, 2629–2637.
- [4] V. Polinger, P. García-Fernández and I. B. Bersuker, *Physica B: Condensed Matter*, 2015, **457**, 296–309.
- [5] I. B. Bersuker, *Appl. Phys. Lett.*, 2015, **106**, 022903.
- [6] I. B. Bersuker, *Chem. Rev.*, 2021, **121**, 1463–1512.
- [7] R. E. Cohen and H. Krakauer, *Ferroelectrics*, 1992, **136**, 65–83.
- [8] R. E. Cohen, *Nature*, 1992, **358**, 136–138.
- [9] J. Junquera and P. Ghosez, *Nature*, 2003, **422**, 506.
- [10] J. M. García-Lastra, P. García-Fernández, F. Calle-Vallejo, A. Trueba, J. A. Aramburu and M. Moreno, *Inorg. Chem.*, 2014, **53**, 6534–6543.

- [11] H. Mirhosseini, I. V. Maznichenko, S. Abdelouahed, S. Ostanin, A. Ernst, I. Mertig and J. Henk, *Phys. Rev. B*, 2010, **81**, 073406.
- [12] Z. Zhong, L. Si, Q. Zhang, W.-G. Yin, S. Yunoki and K. Held, *Adv. Mater. Interfaces*, 2015, **2**, 1400445.
- [13] A. Ali, I. Khan, Z. Ali, F. Khan and I. Ahmad, *Int. J. Mod. Phys. B*, 2019, **33**, 1950231.
- [14] A. Pinczuk, W. Taylor, E. Burstein and I. Lefkowitz, *Solid State Commun.*, 1967, **5**, 429–433.
- [15] A. V. Turik and N. B. Shevchenko, *Phys. Stat. Sol. (B)*, 1979, **95**, 585–592.
- [16] B. Cord and R. Courths, *Surf. Sci.*, 1985, **152-153**, 1141–1146.
- [17] A. F. Carley, P. R. Chalker, J. C. Riviere and M. W. Roberts, *J. Chem. Soc. Faraday Trans. 1*, 1987, **83**, 351–370.
- [18] S. A. Nasser, *Appl. Surf. Sci.*, 2000, **157**, 14–22.
- [19] F. Wan, J. Han and Z. Zhu, *Phys. Lett. A*, 2008, **372**, 2137–2140.
- [20] M. K. Sah, S. Mukherjee, K. Naskar, S. Hazra and S. Adhikari, *Int. J. Quantum Chem.*, 2023, **123**, e27212.
- [21] M. Born and J. R. Oppenheimer, *Ann. Phys. (Leipzig)*, 1927, **84**, 457–84.
- [22] M. Born and K. Huang, *Dynamical Theory of Crystal Lattices*, Oxford University Press, Oxford, 1954.
- [23] I. Last, M. Gilibert and M. Baer, *J. Chem. Phys.*, 1997, **107**, 1451–9.
- [24] R. Baer, D. M. Charutz, R. Kosloff and M. Baer, *J. Chem. Phys.*, 1996, **105**, 9141–52.
- [25] S. Adhikari and G. D. Billing, *J. Chem. Phys.*, 1999, **111**, 40–7.
- [26] A. J. C. Varandas and Z. R. Xu, *J. Chem. Phys.*, 2000, **112**, 2121–7.
- [27] S. Adhikari, G. D. Billing, A. Alijah, S. H. Lin and M. Baer, *Phys. Rev. A*, 2000, **62**, 32507.
- [28] B. Sarkar and S. Adhikari, *J. Chem. Phys.*, 2006, **124**, 074101.
- [29] B. Sarkar and S. Adhikari, *J. Phys. Chem. A*, 2008, **112**, 9868–85.

- [30] A. K. Paul, S. Sardar, B. Sarkar and S. Adhikari, *J. Chem. Phys.*, 2009, **131**, 124312.
- [31] H. Hellmann, *Einführung in die Quantenchemie*, Franz Duetliche:Leipzig, Germany, 1937.
- [32] R. P. Feynmann and A. R. Hibbs, *Quantum Mechanics and Path Integrals*, McCraw-Hill, New York, 1965.
- [33] H. Köppel, W. Domcke and L. S. Cederbaum, *Adv. Chem. Phys.*, 1984, **57**, 59–246.
- [34] A. Thiel and H. Köppel, *J. Chem. Phys.*, 1999, **110**, 9371.
- [35] H. Köppel, J. Gronki and S. Mahapatra, *J. Chem. Phys.*, 2001, **150**, 2377.
- [36] A. Viel, W. Eisfeld, S. Neumann, W. Domcke and U. Manthe, *J. Chem. Phys.*, 2006, **124**, 214306/1–16.
- [37] A. Abedi, N. T. Maitra and E. K. U. Gross, *P. Rev. Lett.*, 2010, **105**, 123002.
- [38] A. Abedi, N. T. Maitra and E. K. U. Gross, *J. Chem. Phys.*, 2012, **137**, 22A530.
- [39] G. A. Worth, H.-D. Meyer, H. Köppel, L. S. Cederbaum and I. Burghardt, *Int. Rev. Phys. Chem.*, 2008, **27**, 569.
- [40] G. W. Richings, I. Polyak, K. Spinlove, G. A. Worth, , I. Burghardt and B. Lasorne, *Int. Rev. Phys. Chem.*, 2015, **34**, 269.
- [41] A. J. C. Varandas, F. B. Brown, C. A. Mead, D. G. Truhlar and N. C. Blais, *J. Chem. Phys.*, 1987, **86**, 6258.
- [42] T. Yonehara, K. Hanasaki and K. Takatsuka, *Chem. Rev.*, 2012, **112**, 499–542.
- [43] K. Takatsuka and T. Yonehara, *Phys. Chem. Chem. Phys.*, 2011, **13**, 4987–5016.
- [44] B. G. Levine and T. J. Martínez, *Annu. Rev. Phys. Chem.*, 2007, **58**, 613.
- [45] B. F. E. Curchod and T. J. Martínez, *Chem. Rev.*, 2018, **118**, 3305–3336.
- [46] F. T. Smith, *Phys. Rev.*, 1969, **179**, 111–23.
- [47] Z. H. Top and M. Baer, *J. Chem. Phys.*, 1977, **66**, 1363.
- [48] M. Baer, *Chem. Phys. Lett.*, 1975, **35**, 112–18.

- [49] M. Baer, *Phys. Rep.*, 2002, **358**, 75.
- [50] M. Baer, *Beyond Born - Oppenheimer: Conical intersections and Electronic nonadiabatic coupling terms*, Wiley Interscience, New Jersey, 2006.
- [51] A. M. Mebel, G. J. Halász, A. Vibók, A. Alijah and M. Baer, *J. Chem. Phys.*, 2002, **117**, 991–1000.
- [52] M. Baer and R. Englman, *Mol. Phys.*, 1992, **75**, 293–303.
- [53] A. Alijah and M. Baer, *J. Phys. Chem. A*, 2000, **104**, 389–96.
- [54] S. Mukherjee, B. Mukherjee and S. Adhikari, *J. Phys. Chem. A*, 2017, **121**, 6314–26.
- [55] S. Mukherjee, J. Dutta, B. Mukherjee, S. Sardar and S. Adhikari, *J. Chem. Phys.*, 2019, **150**, 064308.
- [56] K. Naskar, S. Mukherjee, B. Mukherjee, S. Ravi, S. Mukherjee, S. Sardar and S. Adhikari, *J. Chem. Theory Comput.*, 2020, **16**, 1666–1680.
- [57] S. Mukherjee, S. Bandyopadhyay, A. K. Paul and S. Adhikari, *J. Phys. Chem. A*, 2013, **117**, 3475–95.
- [58] S. Mukherjee and S. Adhikari, *Chem. Phys.*, 2014, **440**, 106–18.
- [59] S. Sardar, S. Mukherjee, A. K. Paul and S. Adhikari, *Chem. Phys.*, 2013, **416**, 11–20.
- [60] S. Mukherjee, B. Mukherjee, S. Sardar and S. Adhikari, *J. Chem. Phys.*, 2015, **143**, 244307.
- [61] B. Mukherjee, S. Mukherjee, S. Sardar, K. R. Shamasundar and S. Adhikari, *Mol. Phys.*, 2017, **115**, 2833–48.
- [62] S. Mukherjee, B. Mukherjee, J. Dutta, S. Sardar and S. Adhikari, *ACS omega*, 2018, **3**, 12465–75.
- [63] B. Mukherjee, S. Mukherjee, S. Sardar, K. R. Shamasundar and S. Adhikari, *Chem. Phys.*, 2018, **515**, 350–9.
- [64] S. Mukherjee, B. Mukherjee, S. Sardar and S. Adhikari, *Comp. Theor. Chem.*, 2019, **1154**, 57–67.

- [65] B. Mukherjee, S. Ghosh and S. Adhikari, *J. Phys.: Conf. Ser.*, 2018, **1148**, 012001.
- [66] B. Mukherjee, K. Naskar, S. Mukherjee, S. Ghosh, T. Sahoo and S. Adhikari, *Int. Rev. Phys. Chem.*, 2019, **38**, 287–341.
- [67] J. Dutta, S. Mukherjee, K. Naskar, S. Ghosh, B. Mukherjee, S. Ravi and S. Adhikari, *Phys. Chem. Chem. Phys. (Perspective)*, 2020, **22**, 27496–27524.
- [68] S. Mukherjee, S. Ravi, K. Naskar, S. Sardar and S. Adhikari, *J. Chem. Phys.*, 2021, **154**, 094306.
- [69] S. Mukherjee, S. Ravi, J. Dutta, S. Sardar and S. Adhikari, *Phys. Chem. Chem. Phys.*, 2022, **24**, 2185–2202.
- [70] S. Hazra, S. Mukherjee, S. Ravi, S. Sardar and S. Adhikari, *ChemPhysChem*, 2022, **23**, e202200482.
- [71] M. K. Sah, S. Mukherjee, S. Saha, K. Naskar and S. Adhikari, *J. Chem. Phys.*, 2023, **159**, 244116.
- [72] S. Mukherjee, K. Naskar, S. Hazra, M. K. Sah and S. Adhikari, *J. Phys.: Conf. Ser.*, 2024, **2769**, 012012.
- [73] J. Dutta, S. Ravi, S. Mukherjee, A. K. Ojha and S. Adhikari, *J. Phys. Chem. A*, 2022, **126**, 691–709.
- [74] S. Mukherjee, D. Mukhopadhyay and S. Adhikari, *J. Chem. Phys.*, 2014, **141**, 204306.
- [75] B. Mukherjee, S. Mukherjee and S. Adhikari, *J. Phys. Conf. Ser.*, 2016, **759**, 012050.
- [76] B. Mukherjee, S. Mukherjee, K. R. Shamasundar and S. Adhikari, *J. Phys. Conf. Ser.*, 2017, **833**, 012004.
- [77] S. Ghosh, S. Mukherjee, B. Mukherjee, S. Mandal, R. Sharma, P. Chaudhury and S. Adhikari, *J. Chem. Phys.*, 2017, **147**, 074105/1–16.
- [78] B. Mukherjee, K. Naskar, S. Mukherjee, S. Ravi, K. R. Shamasundar, D. Mukhopadhyay and S. Adhikari, *J. Chem. Phys.*, 2020, **153**, 174301.

- [79] S. Adhikari and G. D. Billing, *J. Chem. Phys.*, 2000, **113**, 1409.
- [80] P. Puzari, B. Sarkar and S. Adhikari, *J. Chem. Phys.*, 2004, **121**, 707.
- [81] P. Puzari, B. Sarkar and S. Adhikari, *Int. J. Quant. Chem.*, 2005, **105**, 209.
- [82] B. A. Khan, S. Sardar, P. Sarkar and S. Adhikari, *J. Phys. Chem. A*, 2014, **118 (49)**, 11451.
- [83] S. Mandal, S. Ghosh, S. Sardar and S. Adhikari, *Int. Rev. Phys. Chem.*, 2019, **37**, 607–700.
- [84] I. B. Bersuker and V. Polinger, *Condensed Matter*, 2020, **5**, year.
- [85] H.-J. Werner, P. J. Knowles, G. Knizia, F. R. Manby, M. Schütz *et al.*, *MOLPRO, version 2018.1, a package of ab initio programs*, 2018, see <http://www.molpro.net>.
- [86] A. Mahmoud, A. Erba, K. E. El-Kelany, M. Rérat and R. Orlando, *Phys. Rev. B*, 2014, **89**, 045103.
- [87] G. H. Kwei, A. C. Lawson, S. J. L. Billinge and S. W. Cheong, *J. Phys. Chem.*, 1993, **97**, 2368–2377.
- [88] M. Moin, A. W. Anwar, M. Babar, U. Thumu and A. Ali, *Heliyon*, 2024, **10**, e24607.
- [89] G. Herzberg and H. C. Longuet-Higgins, *Discuss Faraday Soc.*, 1963, **35**, 77–82.
- [90] S. Pancharatnam, *Proc. Ind. Acad. Sci. A*, 1956, **44**, 247.
- [91] M. V. Berry, *Proc. R. Soc., Lond. A*, 1984, **392**, 45.
- [92] P. Pertosa, G. Hollinger and F. M. Michel-Calendini, *Phys. Rev. B*, 1978, **18**, 5177–5183.
- [93] M. E. Lines and A. M. Glass, *Principles and applications of ferroelectrics and related materials*, Oxford university press, 2001.
- [94] Y. L. Li, L. E. Cross and L. Q. Chen, *J. Appl. Phys.*, 2005, **98**, 064101.
- [95] V. Polinger, *J. Phys.: Conf. Ser.*, 2013, **428**, 012026.
- [96] W. J. Merz, *Phys. Rev.*, 1949, **76**, 1221–1225.
- [97] R. Baer, D. M. Charutz, R. Kosloff and M. Baer, *J. Chem. Phys.*, 1996, **105**, 9141.

- [98] D. R. Yarkony, *J. Chem. Phys.*, 2001, **114**, 2601–2613.
- [99] M. Barbatti, A. J. A. Aquino and H. Lischka, *J. Phys. Chem. A*, 2005, **109**, 5168–5175.
- [100] S. Sardar, A. K. Paul and S. Adhikari, *J. Chem. Sc.*, 2010, **122**, 491.
- [101] S. Sardar, A. K. Paul and S. Adhikari, *Mol. Phys.*, 2009, **107**, 2467.
- [102] S. Sardar, A. K. Paul, R. Sharma and S. Adhikari, *Int. J. Quantum Chem.*, 2011, **111**, 2741–59.
- [103] S. Sardar, A. K. Paul, R. Sharma and S. Adhikari, *J. Chem. Phys.*, 2009, **130**, 144302.
- [104] S. Sardar and S. Adhikari, *J. Chem. Sci.*, 2012, **124**, 51–8.
- [105] G. D. Billing and S. Adhikari, *Chem. Phys. Lett.*, 2000, **321**, 197.
- [106] B. Barkakaty and S. Adhikari, *J. Chem. Phys.*, 2003, **118**, 5302.
- [107] P. A. M. Dirac, *Proc. Cambridge philos. Soc.*, 1930, **26**, 376.